

Simulating topological tensor networks with Majorana qubits

C. Wille,¹ R. Egger,² J. Eisert,¹ and A. Altland³

¹ Dahlem Center for Complex Quantum Systems, Freie Universität Berlin, D-14195 Berlin, Germany,

² Institut für Theoretische Physik, Heinrich-Heine-Universität, D-40225 Düsseldorf, Germany

³ Institut für Theoretische Physik, Universität zu Köln, Zülpicher Str. 77, D-50937 Köln, Germany

The realization of topological quantum phases of matter remains a key challenge to condensed matter physics and quantum information science. In this work, we demonstrate that progress in this direction can be made by combining concepts of tensor network theory with Majorana device technology. Considering the topological double semion string-net phase as an example, we exploit the fact that the representation of topological phases by tensor networks can be significantly simpler than their description by lattice Hamiltonians. The building blocks defining the tensor network are tailored to realization via simple units of capacitively coupled Majorana bound states. In the case under consideration, this defines a remarkably simple blueprint of a synthetic double semion string-net, and one may be optimistic that the required device technology will be available soon. Our results indicate that the implementation of tensor network structures via mesoscopic quantum devices may define a powerful novel avenue to the realization of synthetic topological quantum matter in general.

I. INTRODUCTION

How can complex, or even topological, states of matter be realized in a physical system under precisely controlled conditions? Both from a conceptual and an applied perspective this is one of the most pressing questions of contemporary physics. Much of the dramatic recent progress in the theory of quantum matter is owed to the identification of a vast spectrum of candidate topological phases of matter. At the same time, only few of these phases have been seen in experiment. Except for the quantum Hall states, and perhaps a few systems promising to harbor \mathbb{Z}_2 -gauge symmetries, long range entangled topological phases of matter remain elusive at this point [1, 2]. This is an unfortunate situation, not only from a condensed matter point of view: Conventional approaches to universal quantum computation based on surface codes [3] require enormous overheads in magic state distillation [4], which may well turn out to be impractical. By contrast, the excitations supported by topological phases of matter have much stronger computational potential [1, 5, 6] and would arguably define a faster pathway, if only they could be realized.

The apparent gap between theoretical understanding and the reality of materials is best illustrated by the concept of string-nets. Proposed more than a decade ago as a theoretical paradigm perhaps large enough to include all (gapped bosonic) topological quantum phases [2, 7, 8], all but the simplest string-net Hamiltonians contain carefully balanced 12-spin interactions. No real life material will deliver such type of effective interactions out of the box. The standard way of reading the situation is to consider the string-net Hamiltonians as effective fixed points inside their topological phases. However, from a pragmatic perspective this only sidesteps the problem, and the identification of the respective basins of attraction in relation to existing quantum matter remains a daunting challenge.

There are two principal approaches to make progress in this situation. The first aims to identify quantum matter in a prospected topological phase without direct reference to the representing string-net fixed point. As indicated above, progress in this direction has been rather limited so far. The

second aims to engineer synthetic string-nets, or better to say simulators of string-nets, from well controlled device building blocks, in the mindset of a quantum simulation [9, 10], together with versatile design principles that allow one to devise complex models from these building blocks.

The present work reports significant progress with respect to the second category. More specifically, our approach is based on the combination of two design principles: Firstly, we present a new application of tensor network theory [11–14]. Tensor networks are known to describe string-nets in ways drastically reduced in complexity compared to the native Hamiltonian. Here, this insight is applied to provide a blueprint how phases of matter can be devised from basic building blocks. Secondly, we propose the realization of these two-dimensional (2D) structures in a hardware platform featuring Majorana bound states [15–26]. Both directions are novel. We emphasize right away that the Majorana qubit introduced in Refs. [27–31] is essential for its unique capability in describing electronic and Pauli spin correlations. However, the hardware overhead required on top of the Majorana states is comparatively modest and does not go beyond that otherwise required to realize small-scale qubit networks. Our design is thus formulated in terms of device technology that is not yet available but with a bit of optimism will be very soon [20].

Tensor networks provide a very natural environment for the description of topological matter, and in particular for string-nets. In fact, the fusion rules of topological quasi-particles find a mathematical abstraction in tensor categories, whose representation in the language of string-nets represents a tensor network almost by design. The formulation of a tensor network involves a ‘physical’ and a ‘virtual’ space, where the former represents physical degrees of freedom (spins on a lattice, etc.) and the second serves to generate entanglement and capture the correlation structure of the state. While the representation of string-net ground states as tensor networks is relatively straightforward [32, 33], a drastic simplification emerges from the idea [34–37] to inject, or encode, the physical space into the larger space of virtual states. In exchange for the seeming redundancy of this encoding, one gains a much simpler local description in terms of an effective

Hamiltonian. At least, it is simple enough to afford a direct realization in quantum devices.

To demonstrate the functioning of the approach introduced, we will illustrate this principle on the case of the double semion string-net [7]. This system comes next in complexity to the elementary toric code. It is not yet universal for quantum computing but already requires the full-feathered machinery of 12-spin correlations on the Hamiltonian level. By passing from physical to virtual space, this complexity gets reduced to a relatively mundane six-spin ring exchange, similar to that, e.g., defining the physical qubits of a toric code on a hexagonal lattice [38]. It is then natural to define the hardware realization of the system with direct reference to the virtual space of the tensor network. To this end, various standard elements of tensor network constructions, e.g., Bell state projections, one-dimensional (1D) matrix product operators (MPOs), or repetition code qubits, all need to be implemented on the device level. A principal observation of this work is that networks of tunnel-coupled low capacitance quantum dots harboring Majorana bound states — Majorana box qubits (MCB) in the jargon of the field [27–31] — are optimally suited to this task.

While this may be true also for more general tensor networks, it certainly is the case for the projected entangled pair state required in our present application. For a preliminary impression of the hardware setup required to realize a double semion string-net, see Fig. 17 below, where the boxes represent MCBs, red and blue lines are tunneling bridges (short quantum wires), and the triangles are mere guides to the eye. (Not shown in the figure are side gates next to the tunneling links required to run a one-time calibration procedure, likewise required in the realization of, e.g., a Majorana surface code [39–42].) We emphasize that the structure does not include elements truly adverse to present-date experimental realization. Specifically, their operation does not require magnetic field interferometry or time varying external voltage sources. The structures rather are static in that the ground state of the tunnel- and capacitively coupled network is the double semion state. AC operations may be required to create anyonic excitations in the system or for the measurement of local state characteristics. However, these are operations beyond the scope of the current text.

In essence, we propose the double semion system as a case study for a conceptually novel avenue to the realization and quantum simulation of topological quantum matter. The approach involves bridging between Hamiltonian and tensor network descriptions of topological matter in a fresh mindset, and from there on to hardware implementations. For the first time, tensor networks are thus not considered as a numerical framework to study interacting quantum matter [11–13], for which tensor network states and in particular projected entangled pair states (PEPS) [43, 44] are well known and for which they have originally been suggested [45]. They are also not used in an a-posteriori approach of capturing complex phases of matter in a mathematically precise and conceptually clear fashion [35–37, 46–49]. Instead, they here serve as immediate candidates for a solid-state device realization. The double semion system is ideally suited to illustrate the principle be-

cause in spite of its relative simplicity, a ‘direct’ realization in quantum matter and/or hardware constructions seems illusive in view of the required 12-spin correlations. The essential insight which brings the system into reach is that its encoding in the virtual space of a tensor network dramatically reduces the complexity required from the hardware. While the generalization to branching string configurations on a lattice is straightforward, the realization of a tensor structure reliably describing a universal phase (such as the double Fibonacci phase) remains a nontrivial task. However, we hope that the concepts and device building blocks introduced below will be instrumental to progress in this direction as well.

The remainder of this work is structured as follows. In Sec. II, we discuss the low-energy theory for arbitrary MCB networks. In particular, we introduce novel design principles based on destructive interference mechanisms, see Sec. IID, which are key to the constructions put forward below. In Sec. III, we show that high-order qubit interactions can be engineered in simple MCB networks based on these design principles. In particular, for 1D structures of coupled MCBs, we establish a link to MPOs and other key elements of tensor network states. Next, after a general discussion of string-nets (in particular, of the double semion system) and their representation in terms of tensor networks in Secs. IVA and IVB, we present the MCB network realization for the ground state of the double semion model in Sec. IVC. This work concludes with an outlook in Sec. V. Technical details related to Sec. IVC can be found in the Appendix.

II. MAJORANA COOPER BOX NETWORKS

In this section we discuss how networks of tunnel coupled Majorana cooper boxes give rise to an effective theory containing engineered many-body interactions. We begin with a review of the smallest unit, the Majorana cooper box (MCB), and then apply perturbation theory to demonstrate how several MCBs connected by tunnel bridges define an effective low energy effective theory. We conclude the section with a discussion of design principles controlling and constraining the correlations present in this network.

A. Majorana Cooper Box

The basic unit on which our approach is based is the Majorana Cooper box (MCB) [27–31]. A single MCB can be conceptualized as a system of mesoscopic size, i labelling spatial sites, harboring an even number $2n$ of spatially localized Majorana bound states (MBSs). The latter correspond to Majorana operators $\gamma_{i,a} = \gamma_{i,a}^\dagger$ with $a = 1, \dots, 2n$ and the anticommutator algebra

$$\{\gamma_{i,a}, \gamma_{j,b}\} = 2\delta_{ij}\delta_{ab}. \quad (1)$$

For recent reviews of MBS physics, see Refs. [15–20]. The upper panel in Fig. 1 shows examples with $n = 2$ and $n = 3$, called *tetron* and *hexon* [31], respectively. The 2^n -dimensional Hilbert space representing each box is split into

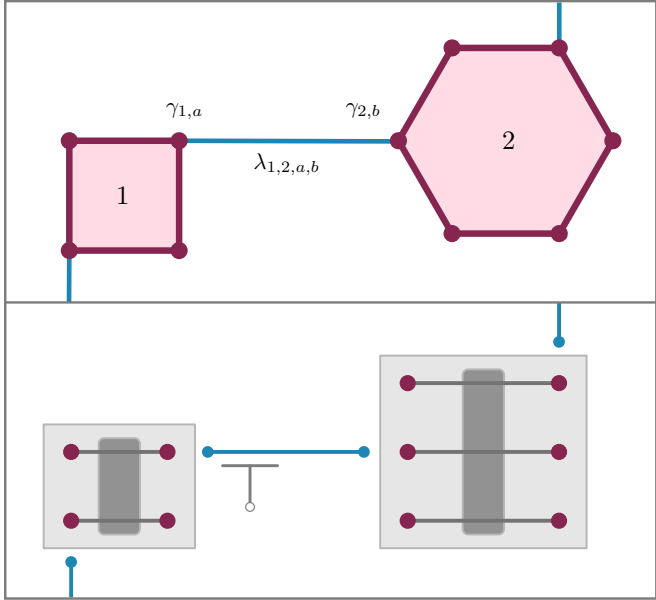


FIG. 1. Upper panel: Part of a network containing one tetron (MCB 1) and one hexon (MCB 2). In the ground state, each MCB abides in a definite eigenstate of the parity operator (2). Individual MBSs of different MCBs are coupled via complex tunneling amplitudes indicated in blue. Bottom panel: A somewhat less schematic representation of the same architecture, emphasizing that each MCB is a mesoscopic island comprising n parallel quantum wires proximitized by the same superconductor (shaded vertical structure). Tunneling links between neighboring MCBs are tunable via local gate voltage changes.

two 2^{n-1} -dimensional subspaces identified by the eigenvalues of the fermion number parity operator,

$$\mathcal{P} = i^n \gamma_1 \dots \gamma_{2n} = \pm 1. \quad (2)$$

The even- and odd-parity sectors are separated by a large energy gap due to the charging energy E_C of the box (see below). Without loss of generality, we assume that the sector $\mathcal{P} = -1$ ($\mathcal{P} = +1$) is energetically favored for every tetron (hexon). The condition (2) implies strong entanglement between the elementary MBSs in each parity sector and will be of crucial importance to the definition of higher levels of entanglement between the base units. Next, Majorana operators $\gamma_{i,a}$ and $\gamma_{j,b}$ belonging to neighboring MCBs i, j may be coupled by tunneling links characterized by tunneling amplitudes $\lambda_{ij,ab}$. Before discussing how the units introduced above can be combined to functional networks [38, 40, 41, 50–54], let us briefly review how they could be realized in practice.

Referring for a detailed discussion to Refs. [30, 31, 39], we note that a $2n$ MCB is a collection of n parallel (semiconductor or topological insulator) quantum wires, all connected to a conventional mesoscopic superconductor. The quantum wires are characterized by strong intrinsic spin-orbit coupling (e.g., InAs or InSb nanowires [20]) and can be fabricated with their own superconducting shell (e.g., an epitaxial Al surface layer [22]). All wires are isolated against ground but electrically connected by the superconductor island to form a float-

ing (not grounded) MCB. A schematic of the setup is shown in the bottom panel of Fig. 1, where the vertical dark shaded bars indicate the superconductor connected to the horizontal wires. The competition of superconductivity, magnetic field, and spin-orbit coupling in the wires drives the system into a topological state whose prime signature is the formation of MBSs at the wire ends [15–20], see for instance Refs. [21–26] for recent experimental reports of MBS signatures in related setups. Since the wires are parallel, a uniform magnetic field along the wire direction will induce the topological transition simultaneously in all wires.

In practice, these MBSs are quantum states of finite extension, and wave function overlap between them should be avoided in order to realize true zero-energy states. However, experiment indicates that for device proportions in the $\mathcal{O}(1\mu\text{m})$ range, this hybridization can be made negligibly small [20, 22]. When isolated against ground, systems of this size have small electrostatic capacitance, C , and as a consequence a large electrostatic charging energy, $E_C(N - n_g)^2$, where $E_C := e^2/2C \approx 1 \text{ meV}$ [22], N is the particle number on the MCB and n_g an effective background parameter tunable via side-gate electrodes. Importantly, charging effects are sensitive to the number of fermions occupying the Majorana sector of the MCB, $n_\gamma = \sum_{\alpha=1}^n n_\alpha$ with $n_\alpha := c_\alpha^\dagger c_\alpha$ and conventional fermion operators $c_\alpha = (\gamma_{2\alpha-1} + i\gamma_{2\alpha})/2$ [55]. In the generic Coulomb valley case, n_g is tuned to a value such that the closest integer, N , is electrostatically favored. In fact, the MCB networks described below are operated at integer values of n_g for all MCBs, where the low-energy theory enjoys particle-hole (anti-)symmetry. In any case, the resulting effective constraint to remain at a specific value of N fixes the parity of n_γ and thus yields Eq. (2) [27, 29, 56]. (Only the parity is fixed because a number of, say, $n_\gamma = 3$ can be converted to $n_\gamma = 1$ by creating a Cooper pair in the superconductor at no energy cost.) Finally, we also assume that the proximity-induced superconducting gap in the wires is sufficiently large to justify the neglect of above-gap quasiparticles.

MCB structures similar to the ones sketched above in design and proportions are currently becoming experimental reality. The formation of MBSs, controllable hybridization between MBSs as well as electrostatic charging effects have been evidenced in a number of reports [21–26]. While we have not yet witnessed controlled Majorana qubit or MBS braiding experiments, these are the next conceptual steps on the agenda. Once these steps have been achieved, and sources of decoherence are under effective control, the construction of networks will come into focus.

B. Tunneling Hamiltonian

Individual MCBs can be connected by placing tunneling bridges between MBSs on different islands, as indicated in blue in Fig. 1. These phase-coherent connectors (e.g., normal-conducting short nanowires) define the effective couplings $\lambda_{ij,ab}$. Their bare values respond sensitively to variations in the fabrication process and may largely be out of control. However, their values can subsequently be tuned via

voltage changes on local side gates, as indicated in the bottom panel of Fig. 1. This freedom may be applied to adjust individual tunneling amplitudes to premeditated values in a one-time interferometric calibration procedure prior to the operation of the system, see Secs. II E and IV C below and Refs. [30, 31, 39, 55]. While current fabrication technology does not exclude crossing links in a quasi-2D architecture [20], they are difficult to implement in practice. The networks described below are constructed such that the number of crossings is kept at a minimum.

Our approach will be based on perturbation theory in the parameters $|\lambda_{ij,ab}|/E_C \ll 1$. Physically, this means that state changes of the system are induced by virtual excitations out of the definite parity ground state sector. The formulation of this expansion is facilitated by turning to a charge fractionalized picture wherein all Majorana fermions are considered electrically neutral and the charge balance is described by a number-phase conjugate pair $[\hat{\varphi}_i, \hat{N}_j] = i\delta_{ij}$ [28, 29, 55]. Technically, the passage to this formulation amounts to a gauge transformation, $c_{i,\alpha} \mapsto c_{i,\alpha} e^{i\hat{\varphi}_i}$, applied to the fermion operators of the respective MCB. When represented in this way, the Hamiltonian of the system assumes the form $\hat{H} = \hat{H}_0 + \hat{H}_t$, where $\hat{H}_0 = E_C \sum_i (\hat{N}_i - n_{g,i})^2$ includes the charging Hamiltonians of all MCBs and \hat{H}_t contains the tunnel couplings connecting different MCBs,

$$\hat{H}_t = \sum_{ij,ab} \lambda_{ij,ab} \gamma_{i,a} \gamma_{j,b} e^{i(\hat{\varphi}_i - \hat{\varphi}_j)} + \text{h.c.} . \quad (3)$$

These operators describe the inter-MCB correlation of Majorana bilinears $\gamma_{i,a} \gamma_{j,b}$ via the tunneling amplitudes $\lambda_{ij,ab}$, where $e^{i(\hat{\varphi}_i - \hat{\varphi}_j)}$ accounts for the fact that charge is raised/lowered by one unit on MCB i/j . Note that the action of \hat{H}_t on the \hat{H}_0 charge ground state generates an excited state. The task of the perturbative program outlined above is the identification of relevant virtual ring-exchange processes wherein multiple tunneling leads back to the ground state.

C. MCB Pauli operators

For our purposes below, it will be convenient to represent bilinears of Majorana operators acting within a sector of definite parity through qubit Pauli operators, that is, $\hat{x}, \hat{y}, \hat{z}$. For example, the ground-state space of a tetron, i.e., the space of two conventional fermions with even parity ($n_\gamma = 0, 2$), is equivalent to the Hilbert space of a single qubit [27]. Indeed, the representation

$$\gamma_1 \gamma_2 = -i\hat{x}, \quad \gamma_2 \gamma_3 = -i\hat{y}, \quad \gamma_1 \gamma_3 = -i\hat{z}, \quad (4)$$

faithfully represents the operator algebra of Majorana bilinears. Combinations involving γ_4 are fixed by the parity constraint in Eq. (2), $\gamma_1 \gamma_2 \gamma_3 \gamma_4 = 1$, as indicated in Fig. 2(a). Since the definite assignment of an Pauli operator equivalence makes reference to a specific ordering of Majorana operators, we occasionally indicate the position of γ_1 by an open circle in our figurative representations.

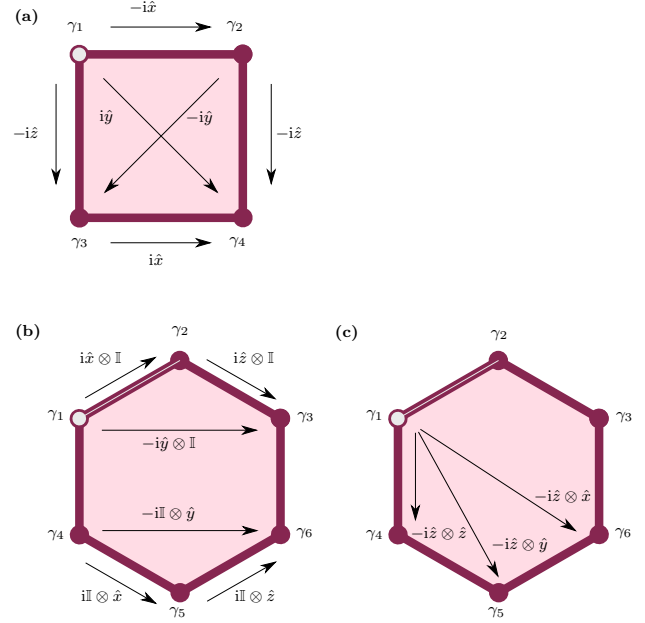


FIG. 2. Pauli operator representation of Majorana bilinears on tetrons and hexons. Arrows between vertices (i.e., MBSs) identify Majorana bilinears and their associated single- or two-qubit operators. The marking of γ_1 (open circle) indicates our Majorana ordering choice. (a) Single-qubit operators for a tetron. (b) Single-qubit operators for a hexon. (c) Several two-qubit operators for a hexon.

For hexons, the ground state space is four-fold degenerate and can be interpreted as the Hilbert space of two qubits [31]. We partition the six MBSs into two groups of three, with the understanding that Majorana bilinears formed from only one group correspond to single-qubit Pauli operators, see Fig. 2(b). In contrast, bilinears involving MBSs from different groups yield two-qubit operators. For instance, $\gamma_1 \gamma_4 = -i\hat{z} \otimes \hat{z}$ follows by using the single-qubit operators in Fig. 2(b) together with the parity constraint in Eq. (2), which for hexons is equivalent to $\gamma_1 \gamma_4 = i\gamma_2 \gamma_3 \gamma_5 \gamma_6$. Several other two-qubit operators are specified in Fig. 2(c).

D. Effective low-energy theory

For a general MCB network Hamiltonian, $\hat{H} = \hat{H}_0 + \hat{H}_t$, each tunneling process involves discharging (charging) the emitting (receiving) MCB by an elementary charge. Since the charging energy E_C is assumed large compared to the tunneling amplitudes, and open tunneling paths inevitably leave the system in an excited state, only *closed paths* are physically relevant to the low-energy physics. In the following we show how Schrieffer-Wolff perturbation theory (taken in the standard self-energy approximation) [57] may be applied to represent the relevant tunneling processes as products of Pauli operators acting on the low-energy Hilbert space of the system. The starting point of Schrieffer-Wolff theory is the series

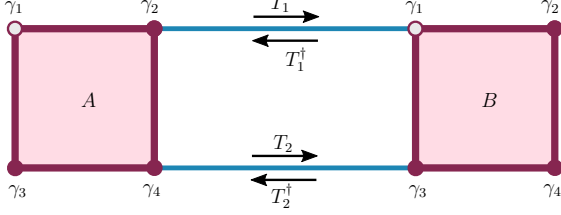


FIG. 3. Example of a minimal MCB network, see Eq. (6).

expansion

$$\hat{H}_{\text{eff}} = \sum_{k=1}^{\infty} \hat{H}^{(k)}, \quad \hat{H}^{(k)} = \hat{P}_0 \left(\hat{H}_t \frac{1}{-\hat{H}_0} \right)^{k-1} \hat{H}_t \hat{P}_0, \quad (5)$$

where \hat{P}_0 is the ground-state projector of \hat{H}_0 .

Let us first discuss the structure of Eq. (5) on the example of two connected tetrions as in Fig. 3. With the notation in Fig. 3, the tunneling Hamiltonian is given by $\hat{H}_t = T_1 + T_2 + T_1^\dagger + T_2^\dagger$ with the hopping operators

$$T_1 = \lambda \gamma_{2,A} \gamma_{1,B} e^{i(\hat{\varphi}_A - \hat{\varphi}_B)}, \quad T_2 = \kappa \gamma_{4,A} \gamma_{3,B} e^{i(\hat{\varphi}_A - \hat{\varphi}_B)}. \quad (6)$$

It is useful to represent individual T_i operators as directed arrows from $\gamma_{i,a}$ to $\gamma_{j,b}$ (for different MCBs $a \neq b$), where Hermitian conjugates T^\dagger correspond to reversed arrows, see Fig. 3. Charge neutrality now requires that each MCB carries an equal number of incoming and outgoing arrows. In this way, terms contributing to Eq. (5) are oriented closed paths and the effective Hamiltonian is given by a sum over all closed paths contributions. We first consider only paths without self-intersections, i.e. oriented loops of length k , where the orientation sense, $d = \pm$, is determined by the arrow direction and briefly remark on self-intersecting closed paths at the end of this section. Since \hat{H}_t is Hermitian, every oriented loop comes along with its Hermitian conjugate counterpart, i.e., a loop with opposite orientation. Moreover, loop contributions to $\hat{H}^{(k)}$ are distinguished by the ordering sequence, s , of individual T_i operators which in general neither commute with each other nor with $1/\hat{H}_0$.

For our two-tetron example in order $k = 2$, we obtain

$$\begin{aligned} \hat{H}^{(2)} &= \hat{O}_{1,2,+}^{(2)} + \hat{O}_{2,1,+}^{(2)} + \hat{O}_{1,2,-}^{(2)} + \hat{O}_{2,1,-}^{(2)}, \\ \hat{O}_{i,j,+}^{(2)} &= \hat{P}_0 T_i \frac{1}{-\hat{H}_0} T_j^\dagger \hat{P}_0, \end{aligned} \quad (7)$$

where the index specifies (s, d) and reversing the loop orientation equals Hermitian conjugation. We note that in Eq. (7) ‘diagonal’ contributions, $\hat{O}_{j,j,\pm}^{(2)}$, have been dropped since they only cause an irrelevant overall energy shift. We now perform the projection to the charge ground state sector in Eq. (7), where the first term takes the form

$$\hat{O}_{1,2,+}^{(2)} = -\frac{\lambda \kappa^*}{2E_C} \gamma_{2,A} \gamma_{1,B} \gamma_{3,B} \gamma_{4,A} = \frac{\lambda \kappa^*}{2E_C} \hat{z}_A \hat{z}_B. \quad (8)$$

Here we have assumed that both MCBs are operated at the electron-hole symmetric point (integer $n_{g,A/B}$). In that case, the intermediate virtual state involves a single-electron charging (decharging) of box A (B) with excitation energy $2E_C$. For the qubit operator representation, i.e., the second equality in Eq. (8), we have used the Pauli operators (4) for each tetron.

We are now ready to specify the general operator structure for an ordered oriented loop of length k ,

$$\hat{O}_{s,d}^{(k)} = i^k A(k, s, d) \hat{Q}^{(k)}, \quad \hat{Q}^{(k)} = \hat{q}_1 \hat{q}_2 \cdots \hat{q}_k, \quad (9)$$

where $\hat{Q}^{(k)}$ is composed of Pauli operators \hat{q}_i acting on MCB i . Note that $\hat{Q}^{(k)}$ neither depends on the orientation d nor on the sequence s . The prefactor $A(k, s, d)$ collects all tunneling amplitudes and the (inverse) excitation energies of virtual intermediate states, with $A(k, s, d) \sim 1/E_C^{k-1}$. Finally, by summing over all possible sequences of T_i operators, we obtain the operator for *unordered* oriented loops,

$$\hat{O}_d^{(k)} = \sum_s \hat{O}_{s,d}^{(k)}. \quad (10)$$

E. Destructive interference mechanisms and Hamiltonian design

Since the prefactor $A(k, s, d)$ in Eq. (9) decays exponentially with the loop length k , dominant contributions to \hat{H}_{eff} originate from short loops involving just a few qubit operators. This fact poses a serious problem for engineering complex quantum systems. In particular, fixed-point Hamiltonians exhibiting topological order, e.g., string-net models, generically rely on the presence of high-order many-qubit interactions [2, 7, 58], see Sec. IV A. A key point of our work is to design MCB network structures where unwanted low-order contributions due to short loops are automatically eliminated by destructive interference.

Based on these design ideas, one can largely tune the effective Hamiltonians in a desired fashion. We expect this to be of general interest for *quantum simulation* beyond the specific application of generating topological models. We next present two different mechanisms effecting such type of loop cancelation.

Loop cancelation by symmetry — Unordered oriented loops will automatically vanish if, for each sequence s of tunneling operators, there exists a *permuted sequence* $\Pi[s]$ with opposite prefactor,

$$A(k, \Pi[s], d) = -A(k, s, d). \quad (11)$$

Indeed, in such cases, Eq. (10) readily gives

$$\hat{O}_d^{(k)} = \sum_s \hat{O}_{s,d}^{(k)} = \sum_s \hat{O}_{\Pi[s],d}^{(k)} = - \sum_s \hat{O}_{s,d}^{(k)} = 0. \quad (12)$$

The next, and more difficult, step is to identify MCB network structures where such loop-canceling permutations exist. To that end, we first observe that for structures containing a pair of anticommuting tunneling operators, $\{T_i, T_j\} = 0$, the prefactor $A(k, s, d)$ will change sign when interchanging T_i and

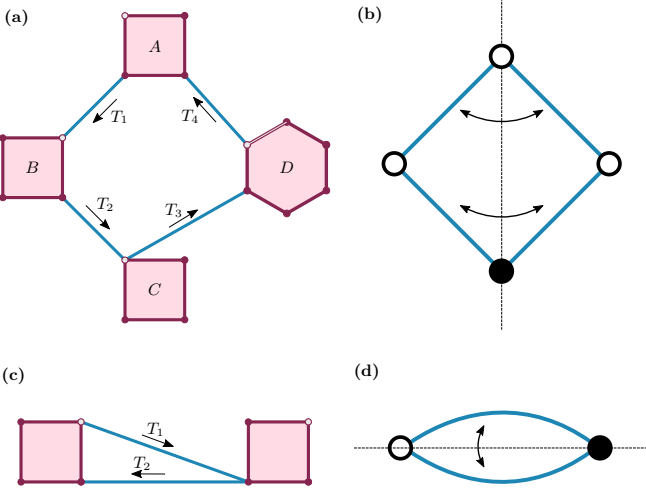


FIG. 4. Two examples for loop cancellation by symmetries and anticommuting T_i terms. (a) MCB network with overlapping hopping terms T_2 and T_3 , and (b) the corresponding reduced graph (see main text for its definition and the coloring of vertices). The reflection symmetry defining the loop-canceling permutation $\Pi[s]$ is also indicated. (c) Another example for a network with anticommuting T_i operators and (d) the associated reduced graph.

T_j in the sequence s . Anticommuting T_i and T_j operators share a common Majorana operator and thus represent *overlapping* hopping terms. Two examples for MCB structures with overlapping T_i operators are depicted in Fig. 4.

However, an odd number of overlapping T_i operator pairs — and thus a sign change in $A(k, s, d)$ for the permuted sequence — is only a necessary (but not sufficient) condition for loop cancellation. In order to fulfill Eq. (11), we also have to guarantee that the product of intermediate excitation energies is identical. The latter are determined by the charging contribution \hat{H}_0 and therefore only depend on the charge transferred between MCBs, irrespective of precisely which MBSs are involved in the tunneling path or whether we have tetrons or hexons. Loop structures with an invariant energy product can then be identified from a simpler *reduced graph* obtained by collapsing each MCB to a single vertex, see Fig. 4(b,d) for examples. For convenience, vertices with overlapping T_i operators are now marked by a different color (black in Fig. 4). If the reduced graph has a reflection symmetry, mapping edges to edges and vertices to vertices of the same color, every sequence s is uniquely mapped onto a mirror sequence with the same energy product. If the reflection symmetry also interchanges an odd number of overlapping T_i pairs, this map defines a loop-canceling permutation $\Pi[s]$.

Let us illustrate this mechanism for the MCB network in Fig. 4(a), which has a reflection symmetry of its reduced graph [see Fig. 4(b)] along the vertical axis. This symmetry corresponds to the permutation $T_1 \leftrightarrow T_4$ and $T_2 \leftrightarrow T_3$ of tunneling terms, with the anticommutator $\{T_2, T_3\} = 0$. Without loss of generality, we set all coupling amplitudes to $\lambda = 1$ and evaluate the $k = 4$ loop contributions for a specific sequence

s and the associated permuted sequence $\Pi[s]$,

$$\begin{aligned}\hat{O}_{s,+}^{(4)} &= \hat{P}_0 T_1 \frac{1}{-\hat{H}_0} T_3 \frac{1}{-\hat{H}_0} T_2 \frac{1}{-\hat{H}_0} T_4 \hat{P}_0 \\ &= \frac{i}{16 E_C^3} \hat{x}_A \hat{x}_B \mathbb{I}_C (\hat{z} \otimes \hat{z})_D , \quad (13) \\ \hat{O}_{\Pi[s],+}^{(4)} &= \hat{P}_0 T_4 \frac{1}{-\hat{H}_0} T_2 \frac{1}{-\hat{H}_0} T_3 \frac{1}{-\hat{H}_0} T_1 \hat{P}_0 \\ &= -\frac{i}{16 E_C^3} \hat{x}_A \hat{x}_B \mathbb{I}_C (\hat{z} \otimes \hat{z})_D .\end{aligned}$$

Clearly, both contributions cancel each other. Such cancellation due to overlapping T_i operators in combination with geometric symmetries already applies at the level of oriented loops. The vanishing of an oriented loop then implies, by Hermitian conjugation, the vanishing of its reversed partner.

Loop cancellation by phase tuning — Alternatively, the cancellation of loops can be achieved via the engineered tuning of complex tunneling couplings, notably their phases. In this way, oriented loops can be converted into anti-Hermitian operators, sign opposite to their reversed partners. The summation over both orientations in Eq. (10) then implies the exact cancellation of the corresponding *unordered unoriented* loop according to

$$\hat{O}^{(k)} = \sum_{d=\pm} \hat{O}_d^{(k)} = \hat{O}_+^{(k)} + \hat{O}_+^{(k)\dagger} = 0 . \quad (14)$$

How the tunneling amplitudes in a given MCB network have to be chosen for this to happen depends on the loop length k . Excluding loop structures containing anticommuting T_i terms, we find that for odd (even) k , the product of all tunneling amplitudes along the loop path has to be purely real (imaginary). In fact, one only needs to tune an overall *loop phase* defined below.

Let us briefly reconsider the two-tetron example in Fig. 3 to illustrate this mechanism. An unordered oriented loop with $k = 2$, winding once around the structure, is described by

$$\hat{O}_+^{(2)} = \frac{\lambda \kappa^*}{E_C} \hat{z}_A \hat{z}_B , \quad (15)$$

cf. Eq. (8). The unoriented loop contribution $\hat{O}^{(2)}$ thus exactly vanishes for $\text{Re}(\lambda \kappa^*) = 0$. Writing $\lambda = |\lambda| e^{i\phi_\lambda}$ and $\kappa = |\kappa| e^{i\phi_\kappa}$, this condition is equivalently formulated as a condition on the loop phase, $\phi_{\text{loop}} := \phi_\lambda - \phi_\kappa = \pm\pi/2$. This type of phase tuning offers a powerful tool for suppressing few-qubit interactions.

We now return to the general case of a length- k loop without anticommuting T_i terms. With the tunneling amplitudes $|\lambda_1| e^{i\phi_1}, \dots, |\lambda_k| e^{i\phi_k}$ along the loop path, the loop phase is $\phi_{\text{loop}} = \phi_1 + \dots + \phi_k$. We then observe that for

$$\phi_{\text{loop}} = \begin{cases} \pm\pi/2 , & k \text{ even} , \\ 0, \pi , & k \text{ odd} , \end{cases} \quad (16)$$

the unoriented loop vanishes, giving rise to $\hat{O}^{(k)} = 0$. In practice, the loop phase may be calibrated in an initial step by adjusting the voltage on just one local gate near a tunneling link

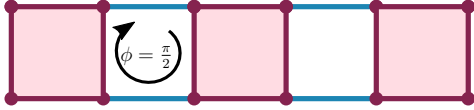


FIG. 5. An example for cancellation of composed loop paths.

within the loop. By means of interferometric (e.g., conductance or capacitance spectroscopy) measurements [30, 31], the value of ϕ_{loop} can be determined experimentally. The local gate voltage is then subsequently readjusted until the desired value of ϕ_{loop} in Eq. (16) has been realized. We expect this calibration technique to be important when building complex structures from elementary building blocks.

Composite loop patterns — Finally, we investigate how the design mechanisms can be transferred to general closed paths. It is straightforward to show that the contribution associated to a disjoint union of loops factorizes into the product of the single loop operators up to a real positive proportionality constant (a combinatorial prefactor) and thus such contributions vanish if one of the loops vanishes. For self-intersecting closed paths cancellation by symmetry is still applicable in the same way as explained above by considering the symmetries of the reduced graph and the sign change of the induced permutation, since the existence of the cancellation permutation Π is not restricted to act on a simple closed loop.

Similarly, we can investigate the elimination of self-intersecting paths by phase tuning. A general oriented closed path with intersections can be partitioned into non-intersecting closed sub-paths. The path is then specified by a collection $\{(d_i, o_i)\}$ of n sub-paths d_i and their orientations, o_i . Due to charge neutrality every such system is equivalent to an assembly of n closed oriented non-intersecting loops. A non-oriented parent path defines all different orientation patterns of its sub-paths. From all possible 2^n orientation patterns only the ones subject to the constraint that the number of paths ending and starting at each vertex is the same have to be considered, since the others are at odds with charge neutrality. If all those patterns are such that they contain at least one oriented loop with canceling loop phase ($\pm\pi/2$ for even or $0, \pi$ for odd length) the parent path is subject to cancellation. For an example, consider the (unoriented) loops in Fig. 5. The left length-2 loop $\hat{L} = \hat{L}_+ + \hat{L}_- = 0$ vanishes due to phase cancellation while the right length-2 loop $\hat{R} = \hat{R}_+ + \hat{R}_-$ has an arbitrary loop phase and does not vanish. The closed path of length-4 $\hat{O}^{(4)}$ obtained by concatenation of \hat{L} and \hat{R} decomposes into two oriented segments, the left and the right loop with clockwise or anticlockwise orientations and thus fulfills the aforementioned criterion. The closed path now be expressed as a sum $\hat{O}^{(4)} = O_{++}^{(4)} + O_{+-}^{(4)} + O_{-+}^{(4)} + O_{--}^{(4)} \propto (\hat{L}_+ + \hat{L}_-)(\hat{R}_+ + \hat{R}_-) = 0$.

III. ENGINEERING MULTI-QUBIT OPERATORS

We next outline how the design principles of Sec. II E may be applied to engineer complex quantum systems with *high-*

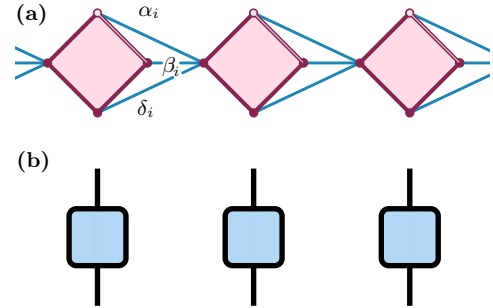


FIG. 6. (a) MCB ring of tetroons (the chain has periodic boundary conditions), and (b) the leading order of the corresponding effective qubit Hamiltonian (17), a product operator, represented as tensor network.

order qubit interactions in MCB networks. In order to design 2D topological models, we have to formulate new design principles to make sure that we arrive at models that are in the anticipated phase. We do so by building upon the framework of Hamiltonian gadgets [59], as will be explained below.

As an intermediate step, we identify design principles for constructing multi-qubit operators. In Sec. IV, these 1D structures will be lifted to give rise to the anticipated topological 2D structures. In this endeavor, *tensor networks* [11–14] will appear, first in 1D structures such as matrix product operators [60–65]. In what follows, we begin by discussing effective Hamiltonians describing rings of M coupled qubits, as in Fig. 6(a) for a tetroon ring. Such structures will later be used as building blocks for the design of 2D Hamiltonians. Specifically, we aim to demonstrate that they may be characterized in terms of MPOs. This picture will be useful in demonstrating the option to generate effective interactions beyond the nearest neighbor level.

A. Product operators

Consider a ring of M coupled MCBs, where tunneling bridges only connect neighboring MCBs. We assume that each MCB contains one MBS at which all tunneling bridges incoming from the left neighbor terminate, as illustrated in Fig. 6(a) for a tetroon ring. In such structures, loop paths not fully winding around the ring necessarily include one sub-loop of length 2. However, these loops vanish by symmetry, as illustrated in Fig. 4(c,d). Thus, composite loops containing one or several length-2 sub-loops vanish as well and we only need to consider loop paths with (one or several) full windings around the ring.

We here focus on loops with a single winding as they contribute dominantly to the perturbation expansion (5). Noting that hopping processes between adjacent MCBs correspond to a sum of Pauli operators weighted by the respective tunneling amplitudes, \hat{q}_i , we obtain the oriented loop operator

$$\hat{O}_+^{(M)} = \frac{-i^M}{(2E_C)^{M-1}} \hat{q}_1 \hat{q}_2 \cdots \hat{q}_M , \quad (17)$$

$$\hat{q}_i = \delta_i \hat{x}_i + \beta_i \hat{y}_i + \alpha_i \hat{z}_i .$$

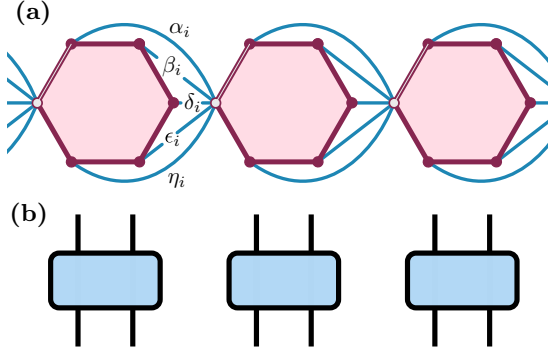


FIG. 7. (a) MCB ring of hexons, and (b) the leading order of its effective qubit Hamiltonian, a product operator composed from two-qubit operators, depicted as tensor network.

The complex constants $\alpha_i, \beta_i, \delta_i$ describe the three tunneling amplitudes connecting the MCB labeled by i to its left neighbor, see Fig. 6(a). We next observe that for loops with even (odd) length M and purely real (imaginary) tunneling amplitudes, $\hat{O}_+^{(M)}$ is Hermitian. In that case, the low-energy Hamiltonian, $\hat{H}_{\text{eff}} = 2\hat{O}_+^{(M)}$, implements a Hermitian product operator of qubits, where the associated tensor network is shown in Fig. 6(b). We also note that by detuning the tunneling phases away from the fine-tuned points above, one may generate operators with stronger entanglement, corresponding to the sum of two product operators.

The above product operator design can also be implemented for hexons or mixed tetro-hexon structures. For hexons, Eq. (17) is still an appropriate description. However, the individual \hat{q}_i operators are now replaced by two-qubit operators. For instance, for the example in Fig. 7(a), we have

$$\begin{aligned} \hat{q}_i = & -\alpha_i(\hat{x} \otimes \mathbb{I})_i + \beta_i(\hat{y} \otimes \mathbb{I})_i \\ & + \delta_i(\hat{z} \otimes \hat{x})_i + \epsilon_i(\hat{z} \otimes \hat{y})_i + \eta_i(\hat{z} \otimes \hat{z})_i, \end{aligned} \quad (18)$$

where the constants $\alpha_i, \beta_i, \delta_i, \epsilon_i, \eta_i$ refer to the five tunneling amplitudes connecting the MCB labeled by i to its left neighbor, see Fig. 7(a). The corresponding tensor network is shown in Fig. 7(b). Since the total operator is just a single product over operators, \hat{q}_i specific to each i (rather than a sum over products), the network does not carry a 'virtual' internal index, as indicated by the absence of horizontal links. The two-qubit nature of the compound operators \hat{q}_i is indicated by the presence of two vertical index lines at each block. More complex structures can be designed by increasing the number of tunneling bridges connecting neighboring MCBs. This idea naturally leads us to MPOs.

B. Matrix product operators

We now consider rings where neighboring MCBs are coupled by tunneling bridges connecting at least two MBSs for each MCB. First consider a tetro ring as in Fig. 8(a). Denot-

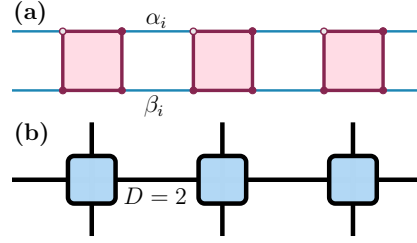


FIG. 8. Matrix product operators. (a) Tetro ring of length $M = 3$. (b) Tensor network representation for case (a) as a qubit MPO. The bond dimension of this MPO is $D = 2$.

ing the tunneling amplitudes of the upper (lower) link by

$$\alpha_i = |\alpha_i| e^{i\phi_{\alpha_i}} \quad (\beta_i = |\beta_i| e^{i\phi_{\beta_i}}), \quad (19)$$

we focus on the option to tune the loop phases,

$$\phi_{\text{loop}}^{(i)} = \phi_{\alpha_i} - \phi_{\beta_i}. \quad (20)$$

Destructive interference occurs for

$$\phi_{\text{loop}}^{(i)} = \pm\pi/2, \quad (21)$$

see Eq. (16). If all $\phi_{\text{loop}}^{(i)}$ are tuned to this value, the leading-order contributions to the series expansion (5) are again loops winding around the ring once. In this case, the effective low energy Hamiltonian representing the structure is given by $\hat{H}_{\text{eff}} = \hat{O}_+^{(M)} + \text{h.c.}$, where the oriented loop operators afford the MPO representation

$$\begin{aligned} \hat{O}_+^{(M)} &= \frac{-i^M}{(2E_C)^{M-1}} \sum_{i_1=0,1} \cdots \sum_{i_M=0,1} \hat{A}_{i_1 i_2}^1 \hat{A}_{i_2 i_3}^2 \cdots \hat{A}_{i_M i_1}^M \\ &= \frac{-i^M}{(2E_C)^{M-1}} \text{Tr} \left(\hat{A}^1 \hat{A}^2 \cdots \hat{A}^M \right), \end{aligned} \quad (22)$$

and the \hat{A}^i are Pauli operators acting on MCB i weighted by tunneling amplitudes,

$$\begin{aligned} \hat{A}_{00}^i &= -\alpha_i \hat{x}, & \hat{A}_{01}^i &= \beta_i \hat{y}, \\ \hat{A}_{10}^i &= \alpha_i \hat{y}, & \hat{A}_{11}^i &= \beta_i \hat{x}. \end{aligned} \quad (23)$$

The equivalent qubit tensor network representation is depicted in Fig. 8(b) where vertical lines indicate the indices $i_k = 0, 1$ and we used Penrose notation, meaning that that index lines without open ends are summed over. Since the index i_k can assume two different values, the bond is said to have bond dimension $D = 2$.

The structure of Eq. (23) does not suffice to realize arbitrary $D = 2$ MPOs. Specifically each of the summands in Eq. (22) is constrained to contain an even number of Pauli- \hat{y} operators. The latter limitations can be addressed by crossing wires. In general one may consider more complex wirings of neighboring tetroons but apart from changes of the local Pauli bases this does not generate additional operator contents. In particular, it is unclear at this stage how MPOs with bond dimension $D > 2$ could be realized without generating 2-body interactions from additional length-2 loops. Future research should address how such limitations can be overcome.

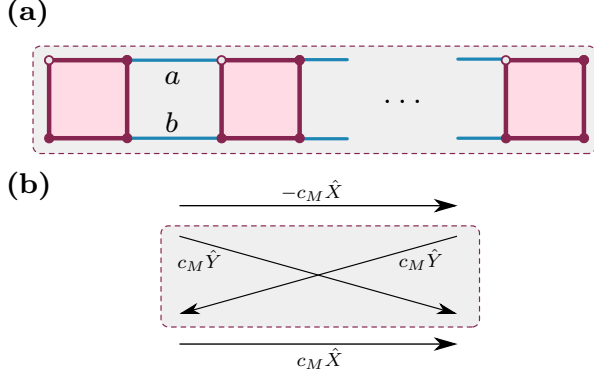


FIG. 9. Logical qubit in a repetition code. (a) Chain of M tetroons with open boundary conditions. Neighboring tetroons are coupled by tunneling amplitudes a and b . (b) Logical Pauli operators \hat{X} and \hat{Y} emerge by pumping an electron through the entire chain, see Eq. (27).

C. Repetition code

We next turn to another useful building block. Consider an open chain of M tetroons, where neighboring tetroons are coupled by two tunneling bridges with amplitudes a and b (assumed identical for all MCB-MCB contacts), see Fig. 9(a). To leading order, \hat{H}_{eff} is determined by summing over all length-2 loops, $\hat{H}_{\text{eff}} \simeq \hat{H}^{(2)}$. The result describes an Ising spin chain,

$$\hat{H}_{\text{eff}} = J \sum_{i=1}^{M-1} \hat{z}_i \hat{z}_{i+1}, \quad J = \frac{\text{Re}(ab^*)}{2E_C}. \quad (24)$$

Tuning all elementary loop phases, $\phi_{\text{loop}} = \phi_a - \phi_b$, such that $\pi/2 < \phi_{\text{loop}} < 3\pi/2$, we have ferromagnetic couplings. The ground state space of the M -qubit chain is then two-fold degenerate and we can encode a logical qubit in this *repetition code* [6]. Interestingly, this logical qubit may be operated just like a single tetron-based qubit but with enhanced error resilience.

To that end, we consider processes where a single electron is pumped through the entire MCB chain. (The practical realization of such a process has been discussed, e.g., in Ref. [40].) We assume that the electron enters the left end of the chain by tunneling in via the MBS located at the top ($j = 0$) or bottom ($j = 1$) left corner of the leftmost MCB. After propagating to the other end, it tunnels out of the chain via the MBS corresponding to the top ($j' = 0$) or bottom ($j' = 1$) right corner of the rightmost MCB. The coherent multi-step tunneling process effectively applies a ‘string operator’ $\hat{S}_{jj'}$ to the M -qubit state, cf. Ref. [40], where $\hat{S}_{jj'}$ is a superposition of Pauli product operators. We now show that the string operators $\hat{S}_{jj'}$, when projected to the ground state space of \hat{H}_{eff} , act like logical \hat{X} and \hat{Y} operators, as indicated in Fig. 9(b).

We first consider the case $M = 2$ with $j = j' = 0$. The corresponding string operator is given by

$$\hat{S}_{00} = \frac{-1}{2E_C} (a\hat{x}_1\hat{x}_2 + b\hat{y}_1\hat{y}_2). \quad (25)$$

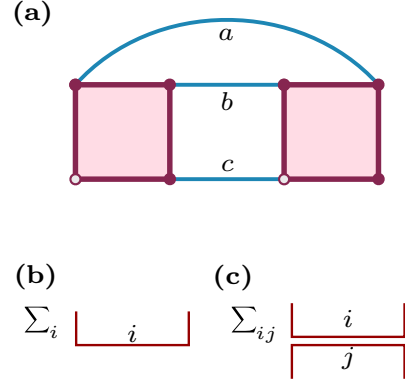


FIG. 10. Bell pairs. (a) Coupled tetron device. The ground state of the associated effective Hamiltonian (29) is a Bell state for real positive $a = b = c$. (b) Tensor network representation of $|\text{Bell}\rangle = |0,0\rangle + |1,1\rangle$. (c) Tensor network representation of the Bell pair projector $\hat{P}_{\text{Bell}} = |\text{Bell}\rangle\langle\text{Bell}|$.

Using $\hat{y} = i\hat{x}\hat{z}$ and $\hat{z}_1\hat{z}_2 = \mathbb{I}_2$ (which holds within the ground-state sector), we obtain

$$\hat{S}_{00} = -\frac{a-b}{2E_C} \hat{x}_1 \hat{x}_2, \quad (26)$$

which is proportional to the logical Pauli- \hat{X} operator. Generalizing this argument now to arbitrary M , logical Pauli operators are defined as $\hat{X} = \hat{x}_1 \hat{x}_2 \cdots \hat{x}_{M-1} \hat{x}_M$ and $\hat{Y} = \hat{x}_1 \cdots \hat{x}_{M-1} \hat{y}_M$. We then find

$$\hat{S}_{00} = -\hat{S}_{11} = -c_M \hat{X}, \quad \hat{S}_{01} = \hat{S}_{10} = c_M \hat{Y}. \quad (27)$$

Apart from the prefactor, $c_M = (-i)^M [(a-b)/(2E_C)]^{M-1}$, this result reproduces the mapping of Majorana bilinears to Pauli operators for a single tetron, cf. Eq. (4).

D. Bell states

We finally show how Bell pair states can be prepared as ground states of tetron structures with tunneling bridges as indicated in Fig. 10(a). Bell states are pairs of maximally entangled qubits, e.g., $|\text{Bell}\rangle = |0,0\rangle + |1,1\rangle$. They are key to tensor network constructs like matrix product states (MPS) and their 2D generalizations, PEPS, see Fig. 10(b). With the projector $\hat{P}_{\text{Bell}} = |\text{Bell}\rangle\langle\text{Bell}|$, see Fig. 10(c), the Hamiltonian

$$\hat{H}_{\text{Bell}} = \varepsilon (1 - \hat{P}_{\text{Bell}}), \quad (28)$$

$\varepsilon > 0$, has $|\text{Bell}\rangle$ as its unique ground state. This Hamiltonian can be realized with two coupled tetroons where a possible setup is shown in Fig. 10(a). We assume that gate calibration has been applied to tune the tunneling amplitudes to real positive values $a = b = c > 0$. In this case, the low-energy Hamiltonian obtained by summation over all length-2 loops reads

$$\hat{H}_{\text{eff}} = \frac{a^2}{2E_C} (-\hat{x}_1 \hat{x}_2 - \hat{z}_1 \hat{z}_2 + \hat{y}_1 \hat{y}_2). \quad (29)$$

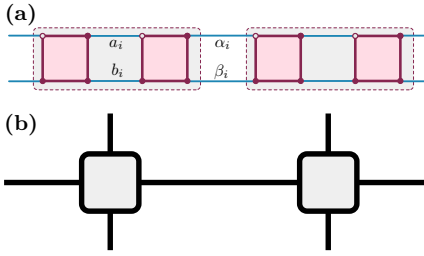


FIG. 11. (a) A hierarchical structure in which units of two tetrons are first linked by tunneling amplitudes $a_i \simeq -b_i$ to define repetition qubits. These blocks are then coupled by amplitudes α_i, β_i to an MPO depicted as tensor network in (b).

This Hamiltonian has $|\text{Bell}\rangle$ as ground state and, for sufficiently strong coupling $\varepsilon = a^2/2E_C$, effectively projects onto this state.

E. Synthesizing design structures

Since the above structures all make reference to sequential ordering, chains of alternating coupling types may be used to define structures containing several types of functionality. As an example relevant to our construction below we mention MPOs whose base units are repetition code qubits. These are formed (see Fig. 11) by first linking blocks of two tetrons each via tunneling amplitudes $\text{Re}(a_i b_i^*) < 0$. This ferromagnetic coupling defines low energy repetition code qubits on the two tetron compounds. These units may then be coupled by amplitudes α_i, β_i to form an MPO structure whose operator units act in the Hilbert spaces of the repetition code qubits.

IV. SIMULATING TOPOLOGICAL TENSOR NETWORKS

The MCB networks discussed in Secs. II and III allow one to realize topological phases with strong entanglement. While previous work has shown that Kitaev’s toric code can be simulated with such constructions [39–42], it has so far remained open how to realize more complicated string-net models. Using the PEPS tensor network representation for the ground states of string-nets, we here discuss how the simplest case beyond Kitaev’s toric code, the *double semion model* [7, 32, 66], can be implemented in a 2D network of MCBs. For pedagogical introductions to tensor networks and PEPS we refer to one of several available reviews, e.g. Ref. [11]. While this will provide useful background knowledge, familiarity with these concepts is not essential throughout as all required material is introduced in a self contained manner. We are confident that by using similar strategies, one could also realize more complicated string-nets such as the Fibonacci Levin-Wen model [7] where, in particular, branching is allowed, and which leads to schemes of universal topological quantum computing. Our approach relates MPOs to MCB networks where destructive interference mechanisms are exploited to suppress short loop contributions. The latter, if present, would drive the system

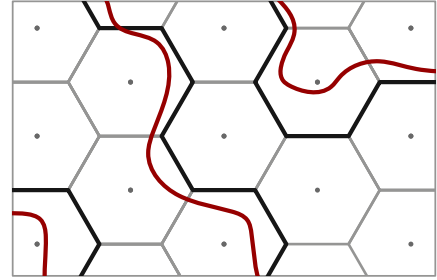


FIG. 12. Black lines: configuration of a non-branching colorless string-net on a trivalent lattice. Red lines: equivalent configuration on the corresponding fat lattice.

into a topologically trivial phase.

To set the stage, we review the basic properties of topological tensor networks from a string-net perspective in Sec. IV A. The Hamiltonian design builds upon seminal work on *Hamiltonian gadgets* [59] which proposed a perturbative approach to topological tensor networks on the abstract level of qubits. The PEPS tensor network used in such a construction will be discussed in Sec. IV B. Finally, the MCB network implementation of the PEPS tensor network realizing the double semion ground state will be presented in Sec. IV C.

A. PEPS representation of string-net ground states

String nets have been introduced in Ref. [7] as generalizations of Kitaev’s toric code and quantum doubles [67], see also Refs. [2, 58, 68, 69]. While the physical idea behind string-nets is relatively easy to communicate in textual or graphical ways, quantitative formulations via formulae tend to be cumbersome. The same is true for the representation of string-net ground states as tensor network states. We therefore begin our discussion of the double semion ground states and its simulation in an MCB network with a qualitative discussion of the main principles along the lines of Refs. [32, 33]. The language is geared to readers with a background in condensed matter physics for which the tensor network approach to topological phases may be less familiar. Throughout, we dispense with technical rigor in exchange for brevity and transparency. For the sake of clarity, parts of our discussion below are formulated in a general language, before specializing to the double semion case.

String net definition — The basis states of a string-net are coverings of a lattice, often chosen as trivalent for convenience, cf. Fig. 12. Complex string-nets allow for coverings carrying N internal indices (‘colors’) i , and senses of directions, i vs. i^* . However, the simple representatives considered here are un-directed and colorless, implying that a covered link may be identified by the label ‘1’, while an empty or vacuum link is identified as ‘0’. We also exclude branching configurations so that the states of the system assume a form as indicated by the pattern of black lines in the figure. For later reference, we denote the linear spaces spanned by N

color indices plus vacuum by $\tilde{V} \simeq \mathbb{C}^{N+1}$.

The physically relevant wave functions, Ψ , defined over these sets of basis states are required to satisfy certain equivalence relations. Referring for a full list of five equivalences to Ref. [7], we note that wave functions are to be invariant under topology-preserving deformations (no crossing or tearing) of lines in the net. The inclusion of a closed, simply contractible loop is equivalent to the multiplication of the wave function by a factor d_i , which for a general net depends on the color i , of the included loop and defines the quantum dimension of the included link species. However, the most important rule describes what happens under local topology changing re-connections of the net. For a general multi-color string-net with orientation, it states that

$$\Psi \left(\begin{array}{c} | \\ | \\ i \\ m \\ k \\ | \\ j \\ l \end{array} \right) = \sum_n F_{lkn}^{ijm} \Psi \left(\begin{array}{c} | \\ | \\ i \\ k \\ n \\ | \\ j \\ l \end{array} \right), \quad (30)$$

where the *F-symbols* are scalar coefficients defining the permissible equivalence reconnections of the net [7].

A non-trivial consistent solution $\{F_{lkn}^{ijm}, d_i\}$ of all consistency relations defines a topological phase. In the present, colorless, non-oriented, non-branching case, there exist only two solutions, the Kitaev toric code, $d_1 = 1$, and the double-semion phase, $d_1 = -1$. Since the nets are non-branching, the *F*-symbols are defined through just one non-trivial reconnection rule,

$$\Psi \left(\begin{array}{c} | \\ | \\ i \\ | \\ j \end{array} \right) = F_{110}^{110} \Psi \left(\begin{array}{c} | \\ | \\ | \\ | \end{array} \right) \quad (31)$$

with $F_{110}^{110} = \pm 1$, respectively. All other *F*-symbols describing permissible non-branching re-connections (for example, F_{111}^{000}) assume the trivial value unity.

From a condensed matter perspective, it may be most natural to describe a string-net in terms of an effective ('fixed point') Hamiltonian

$$\hat{H} = - \sum_v \hat{Q}_v - \sum_p \hat{B}_p, \quad (32)$$

whose eigenfunctions satisfy the above equivalence relations. Here, \hat{Q}_v is a projector onto the permissible configurations at each vertex v , i.e., a projector enforcing total even spin 0, 1 of the adjacent legs in an identification $(0, 1) \leftrightarrow (-1/2, +1/2)$, and \hat{B}_p is an operator specific to the plaquette, p , giving the net dynamics. While the explicit description of \hat{B}_p in terms of *F*-symbols (the product of six symbols depending on the twelve link states of the plaquette and its adjacent legs) or Pauli spin operators (the tensor product of 12 Pauli operators) is both cumbersome and non-intuitive, a much more intuitive description engages the concept of loop insertion on the 'fat lattice'. In fact, the PEPS construction below and its hardware implementation are closer in spirit to this latter formulation than to the Hamiltonian approach.

Fat lattice and PEPS string-net representation — To obtain the fat lattice, consider the width of the 'physical' honeycomb lattice links in Fig. 12 enhanced until the entire plane

is covered except for the plaquette center points. Equivalently, it is a planar structure into which holes are drilled at the plaquette centers. A string-net configuration can now be represented in more relaxed ways, as indicated by the red lines. In our tensor network constructions below, state indices $a, b, \dots = 0, \dots, N$, carried by lines on the fat lattice, will assume the role of 'virtual indices' and we denote the space of these indices by $V \simeq \mathbb{C}^{N+1}$. The distinction from the space \tilde{V} of indices on the physical lattice, $i, j, \dots = 0, \dots, N$, is purely syntactic and introduced for conceptual clarity; physically, there is no difference between lines on the physical or fat lattice.

The advantage of this reformulation is that it allows for a more flexible representation of configuration rearrangements via *F-moves*. Specifically, the fat lattice affords an intuitive definition of the string-net Hamiltonian. To this end, we note that the insertion of a full set of non-vacuum closed loops \hat{B}_p^a ($a = 1, \dots, N$) around a hole p in the fat lattice,

$$\hat{B}_p := \frac{1}{\mathcal{D}^2} \sum_a d_a \hat{B}_p^a \quad (33)$$

with $\mathcal{D}^2 = \sum_{a=1}^N d_a^2$, is a projective operation [7]. The sum of all these operations *defines* the second term, $-\sum_p \hat{B}_p$, of the string-net Hamiltonian. An operation of three sequential *F-moves* may then be applied to represent the Hamiltonian entirely through its action on basis states on the physical lattice [7]. The latter are defined through a configuration i_l of states $i = 0, \dots, N$ specific to lattice links l , and represented in this way the loop insertion assumes the form of a product of six *F*-tensors acting on the link states of the plaquettes surrounding individual loop insertion points. (Following a standard convention we label string types on the fat/physical lattice by $a/i = 0, \dots, N$. This distinction will become useful below when these indices correspond to virtual/physical indices of the tensor network framework.)

In the tensor network description, it is more natural to focus on the Hamiltonian's ground states rather than on the Hamiltonian itself. A ground state must be invariant under the projective action of the Hamiltonian. The projector property implies that, starting from a loopless fat lattice vacuum state $|0\rangle$, a ground state is obtained as $|\text{GS}\rangle = \prod_p \hat{B}_p |0\rangle$, i.e., as an equal weight linear combination of all possible fat lattice elementary loop insertions, see Fig. 13, left. Once again, an operation of sequential *F-moves* may be applied to transform the fat lattice ground state to an equivalent one defined entirely on the physical lattice [32, 33]: in a first step, three *F-moves* specific to each vertex are applied to turn the configuration to the hybrid shown in Fig. 13, center, where the blue dots on the links indicate that the physical lattice is now carrying index structure. This is followed by two more *F-moves* removing all links in the fat lattice and reducing the state to one on the physical lattice. In this final stage, the state assumes the symbolic form $|\text{GS}\rangle = \sum_{\{i\}} C_{\{i\}} |\{i\}\rangle$, where $\{i\}$ is a basis configuration on the physical lattice specified by a set of indices i_l , and the coefficients $C_{\{i\}}$ contain an internal summation over configurations $\{a\}$ originally inserted on the fat lattice. By definition, this makes $C_{\{i\}}$ a tensor network with physical indices

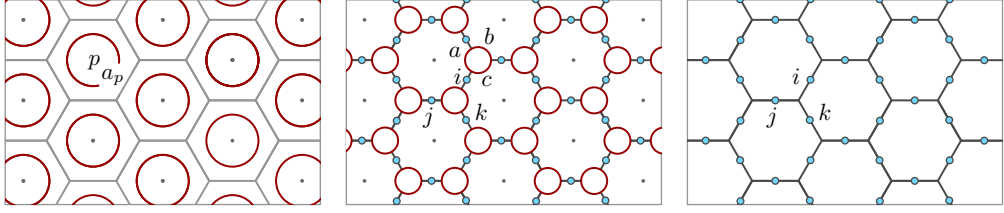


FIG. 13. Left: Ground state of a string-net Hamiltonian as superposition of fat lattice loop insertions. Middle: A hybrid fat/physical lattice representation obtained after a combination of F -moves applied at each lattice center. Right: Full reduction to a physical lattice configuration after reduction of the loops by further F -moves.

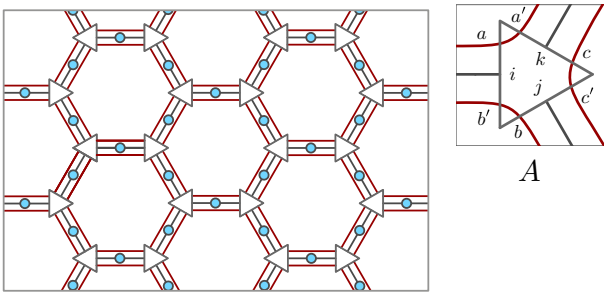


FIG. 14. Representation of string-net ground state as a tensor network. Vertices of the net carry a tensor A .

$\{i\}$ and virtual indices $\{a\}$. The algebraic representation of $C_{\{i\}}$ for a generic string-net is complicated and contains the F -symbols representing the tensorial structure of individual vertices. Individual of these tensors, represented as triangles in Fig. 14, are maps $A^{(ijk)} : V \otimes V \otimes V \mapsto V \otimes V \otimes V$ characterized by tensor components $A_{abc,a'b'c'}^{(ijk)}$. (It may be worth repeating that the only distinction between ‘physical’ (i, j, k) and ‘virtual’ (a, b, c) indices is that the former/latter refer to string states on the physical/fat lattice.) Individual tensor components are defined by F -symbols, where details depend on which sublattice (1, corner triangle right, or 2, corner triangle left) the tensor lives [32, 33]:

$$\begin{aligned} 1 : \quad & A_{abc,a'b'c'}^{(ijk)} = F_{j^*ck}^{a^*ib} \delta_{aa'} \delta_{bb'} \delta_{cc'} , \\ 2 : \quad & A_{abc,a'b'c'}^{(ijk)} = \sqrt{d_j} F_{kai}^{b^*jc} \delta_{aa'} \delta_{bb'} \delta_{cc'} . \end{aligned}$$

Note the presence of the virtual space Kronecker- δ 's which motivates a representation in which the red virtual lines penetrate the tensorial structure.

The representation simplifies further in the case of colorless non-branching nets. The absence of branching reconnections implies a locking between virtual and physical indices, and the configuration (a, b, c) determines that of (i, j, k) . Specifically, in the double semion system the A -tensors of both sublattices

are defined as [32]

$$\begin{aligned} A_{abc,a'b'c'}^{(ijk)} &= A_{abc} \delta_{aa'} \delta_{bb'} \delta_{cc'} , \\ A_{abc} &= \begin{cases} 1 , & a + b + c = 0, 3 , \\ i , & a + b + c = 1 , \\ -i , & a + b + c = 2 . \end{cases} \end{aligned} \quad (34)$$

Implicit to this equation is a locking $i = 1$ if (a, b') have odd parity [(0, 1) or (1, 0)] and 0 else. This replacement rule affords an intuitive interpretation [32]: the ground state of the double semion system is a superposition of all closed loops on the physical lattice, where the coefficient of individual terms is given by the parity $(-)^{\text{no. of loops}}$. The above virtual/physical index locking implies that physical lattice loops are *domain walls* separating hexagons surrounded by virtual loops from those without. The assignment of $\pm i$ and 1 to different virtual index configurations makes sure that each closed domain wall/loop carries the appropriate sign factor.

This concludes our discussion of the PEPS representation of string-nets. In the next subsection we will explore how the above effective mapping of the description from physical to virtual space provides the key to efficient hardware blueprints simulating string-net ground states.

B. Encoded projected entangled pair states

As outlined in the previous subsection, string-net models are naturally described using tensor networks. An attractive feature of this representation is that each of the tensors A contains the full information on the system's topological states. At the same time they define a passage from the space of physical indices into the larger space of virtual indices. The advantage gained in exchange for this redundant encoding of information in a larger space is the option of a more local and hardware friendly description of the system. In this subsection, we show how the translation to an encoded description in virtual space is achieved in concrete ways. And in the next, how it is realized as a concrete MCB hardware layout.

The tensors A define maps,

$$\hat{A} = \sum_{a'b'c', abc, ijk} |i, j, k\rangle A_{abc,a'b'c'}^{(ijk)} \langle a, a', b, b', c, c'| , \quad (35)$$

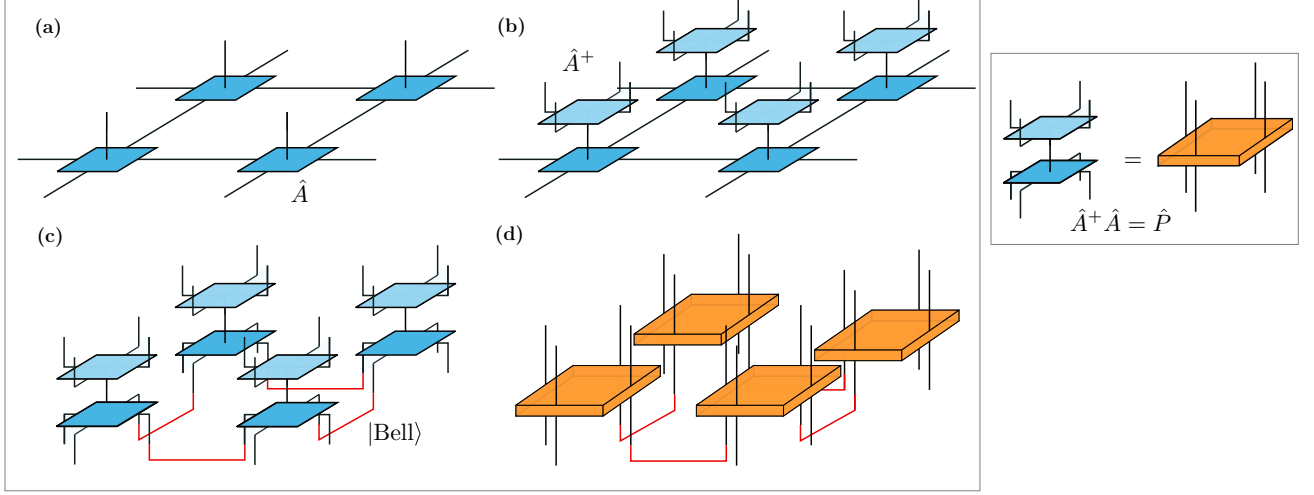


FIG. 15. Topological PEPS on a square lattice. (a) PEPS built from local tensors A . (b) Encoded PEPS obtained by acting with the pseudo-inverse \hat{A}^+ at every physical site, cf. Eq. (37). (c) Encoded PEPS where the deformation of the virtual index lines emphasizes the local presence of Bell pairs shown in red, cf. Fig. 10(b). (d) Encoded PEPS where $\hat{A}^+ \hat{A}$ has been replaced by the projector \hat{P} (panel to the right) at every site.

between the 2^6 -dimensional virtual space, $\otimes^6 V$, and the 2^3 -dimensional physical space, $\otimes^3 \tilde{V}$. Due to the different dimensionality of the spaces, they are neither injective nor invertible. However, to each map \hat{A} there exists a pseudo-inverse \hat{A}^+ defined by the condition

$$\hat{A}^+ \hat{A} = \hat{P} : \otimes^6 V \mapsto \otimes^6 V , \quad (36)$$

where \hat{P} is a projector onto a virtual subspace which is in one-to-one correspondence to the physical space. We will refer to this space as local *code space*. Important properties of this map include $\hat{A}^+ \hat{A} \hat{A}^+ = \hat{A}^+$, meaning that states in the image of \hat{A}^+ are invariant under application of the projector, and similarly, $\hat{A} \hat{A}^+ \hat{A} = \hat{A}$. For a more detailed discussion on the properties of *topological PEPS*, see Refs. [35, 65, 70, 71].

Application of the pseudo-inverse to every physical site of the PEPS ground state yields a state

$$|\Psi'\rangle = \hat{A}^+ \otimes \dots \otimes \hat{A}^+ |\Psi\rangle \quad (37)$$

defined in the larger virtual space. The physical information is now encoded and, following Ref. [59], we call $|\Psi'\rangle$ the *encoded PEPS*. The motivation behind Eq. (37) is that the encoded state will be easier to realize in a physical system. We emphasize again that the un-encoded string-net PEPS, $|\Psi\rangle$, is the ground state of a 12-body Hamiltonian which is extremely difficult to realize in an actual physical system. In contrast the encoded PEPS, $|\Psi'\rangle$, can be obtained perturbatively from a comparatively simple Hamiltonian.

To understand the state $|\Psi'\rangle$ and the alluded Hamiltonian, consider the diagrammatic representation in Fig. 15 where we show a square lattice for better visibility. Following standard tensor network notation, horizontal (perpendicular) lines in panel (a) represent contracted virtual (uncontracted physical)

indices. Each square indicates the local presence of \hat{A} . Now contract each \hat{A} with its pseudo-inverse, see panel (b). The local building blocks now define the projectors \hat{P} (see panel on the right), and this leads to the representation in panels (c) and (d). The visualization emphasizes that this state literally is a PEPS, i.e., a state obtained by the local action of projectors $\hat{P} = \hat{A}^+ \hat{A}$ on an assembly of maximally entangled Bell pairs defined on the links of the lattice.

The entire construction has now been shifted to virtual space. Due to the projective nature of $\hat{P} = \hat{A}^+ \hat{A}$, the encoded state is a ground state of the Hamiltonian

$$\hat{H}' = \sum_v (1 - \hat{P}) + \varepsilon \sum_e (1 - \hat{P}_{\text{Bell}}) , \quad (38)$$

where v runs over the vertices and e over the edges of the underlying lattice, cf. Eq. (28) with $\varepsilon > 0$. This Hamiltonian is referred to as the *perturbative parent Hamiltonian*. The first summands ensure that the low energy states lie within the codes space and thus can be mapped back to the original physical state $|\Psi\rangle$. The Bell pair projections act as a perturbation within this (highly degenerate) ground state and effectively reassemble encoded versions of the original string-net Hamiltonian order by order in a (Schrieffer-Wolff type) perturbation series expansion. For further details we refer to Ref. [59]. For an intuitive relation between the original string-net Hamiltonian and the perturbative PEPS parent, we note that the perturbative expansion in the Bell pair projectors, \hat{P}_{Bell} , contains a ring exchange processes depicted in Fig. 15(d). Much like the toric code ground state can be obtained via the action of all plaquette operators on a vacuum state, the ground state of \hat{H}' is obtained by the action of the ring exchange operators on all virtual lattice loops.

Regarding a hardware design realizing a topological ground

state our problem is thus reduced to that of understanding the local action of $\hat{A}^+ \hat{A}$ and obtaining a good hardware representation of these operators locally. For the concrete case of the double semion model, the A tensors as defined by Eq. (34) is given by

$$\hat{A} = \sum_{abc} |a \oplus b, b \oplus c, c \oplus a\rangle A_{abc} \langle a, a, b, b, c, c| , \quad (39)$$

where the addition modulo two, \oplus , determines physical indices as required by Eq. (34), $i = a \oplus b$, and so on. In this case, the pseudo-inverse has a particularly simple form, $\hat{A}^+ = \frac{1}{2} \hat{A}^\dagger$, where an explicit representation is given by

$$\hat{A}^+ = \frac{1}{2} \sum_{ija} |a, a, a \oplus i, a \oplus i, a \oplus j, a \oplus j\rangle A_{a(a \oplus i)(a \oplus j)}^* \langle j, i \oplus j, i| . \quad (40)$$

Equation (40) states that the pseudo-inverse will map a general physical state of the system, $|j, i \oplus j, i\rangle$, back to a superposition of virtual states subject to the condition that they (i) have pairwise even parity at the corners and (ii) the parity between states at different corners is determined by the physical state of their edge. This leaves only one free summation index, a , while all others are fixed as indicated.

By a straightforward calculation, we obtain the state projectors as

$$\hat{P} = \frac{1}{2} (\hat{P}_c + \hat{X}) , \quad (41)$$

where $\hat{P}_c = \sum_{a,b,c} |a, a, b, b, c, c\rangle \langle a, a, b, b, c, c|$ projects from the 2^6 -dimensional space $\otimes^6 V$ of general states, $|a, a', b, b', c, c'\rangle$, onto the 2^3 -dimensional space of pairwise even-parity states $\simeq \otimes^3 V$. The second operator,

$$\hat{X} = \sum_{abc} |a \oplus 1, a \oplus 1, b \oplus 1, b \oplus 1, c \oplus 1, c \oplus 1\rangle X_{abc} \langle a, a, b, b, c, c| \quad (42)$$

likewise acts in $\otimes^3 V$ where it flips all states and assigns a sign factor

$$X_{abc} = \begin{cases} -1 , & a + b + c = 1, 2 , \\ 1 , & \text{otherwise} . \end{cases} \quad (43)$$

The operator \hat{X} in Eq. (42) can alternatively be represented as MPO with bond dimension $D = 2$,

$$\hat{X} = -\frac{1}{32} \sum_{ijk} \hat{A}_{ij} \otimes \hat{A}_{jk} \otimes \hat{A}_{ki} , \quad (44)$$

where individual factors,

$$\begin{aligned} \hat{A}_{00} &= \hat{A}_{11} = \hat{x} \otimes \hat{x} - \hat{y} \otimes \hat{y} , \\ \hat{A}_{01} &= \hat{A}_{10} = \hat{x} \otimes \hat{y} + \hat{y} \otimes \hat{x} , \end{aligned} \quad (45)$$

act on a qubit pair carried by each of the three corners of the triangular vertex in Fig. 14. In passing we note that the representation of the site-local projector $\hat{A}^+ \hat{A}$ via a local MPO

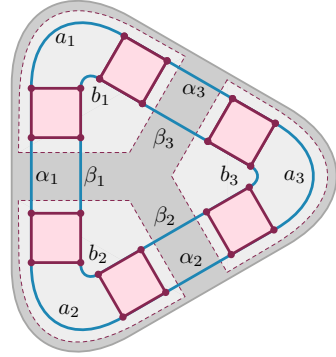


FIG. 16. Tetron ring ('triangle') used for implementing the effective vertex Hamiltonian, \hat{H}_v .

ring contraction reflects the idea of 'MPO injectivity' introduced in Refs. [35, 71]. The advantage of this representation is that the operators \hat{A}_{ij} act like logical Pauli operators on corner qubit pairs, effectively implementing the logical qubit of a repetition code, see Sec. III C.

Since \hat{P}_c acts as an identity operator within the parity subspace $\otimes^3 V$, the essential information on \hat{P} is carried by \hat{X} . Specifically, we know that the local ground space of the operators $1 - \hat{P}$ in the parent Hamiltonian in Eq. (38) coincides with that of $-\hat{X}$. Our objective in the next subsection will thus be to engineer an MCB network whose ground space equals that of $-\hat{X}$.

C. Double semion MCB network

Above, we have identified the operator \hat{X} , Eq. (44), as key to the description of the PEPS ground state. The local action of \hat{X} amounts to an exchange of the three virtual string labels a, b, c in Fig. 14 and the introduction of a sign factor, see Eqs. (42) and (43). This operator can be realized as the tetron ring structure ('triangle') of Fig. 16. In a second step, adjacent triangles are connected via Bell pair tunneling bridges, resulting in the MCB network depicted in Fig. 17. This network has the same ground state as the double semion string-net.

Vertex Hamiltonian — Let us first discuss how the MCB structure shown in Fig. 16 effectively implements the action of the operator \hat{X} at the vertices of the lattice. This six tetron structure defines a three unit repetition qubit MPO in the sense of Sec. III E. The three two-tetron blocks at the corners are linked by tunneling amplitudes (all defined to represent hopping in counter clockwise direction) $a_i \simeq -b_i$. As discussed in Sec. III C, this defines three repetition qubits at the corners. Equivalently, we may say that the elementary length two tunneling loops define operators $\frac{\text{Re}(a_i b_i^*)}{2E_C} \hat{z} \otimes \hat{z}$, where the two factor Pauli operators are defined to act in the Hilbert spaces of the incoming and outgoing virtual states ($|a\rangle$ and $|a'\rangle$, etc., in Fig. 14). In this way, the ground state of the system implies the parity projection $|a\rangle = |a'\rangle$ central to the action of \hat{X} .

The links α_i, β_i couple different repetition qubits. The minimal loops formed from these couplings generate an operator

$\frac{\text{Re}(\alpha_i \beta_i^*)}{2E_C} \hat{z} \otimes \hat{z}$, where the two factor Pauli operators act in the Hilbert spaces of virtual states $|a\rangle$ and $|b\rangle$. Recall that the parity of the latter determines the physical state $|i\rangle = |a \oplus b\rangle$ which is no longer represented by an actual hardware degree of freedom, but can always be deduced from the virtual states. Thus, any preferred alignment of the two spins constitutes an unwanted bias to the code space. to a product state of $|i\rangle = |0\rangle$ at every site. We thus use the freedom to choose $\alpha = i\beta$ and effectively suppress these terms.

The most interesting contribution to the tunneling expansion are the length-6 loops around the ring. Following the same logics as in Sec. III B, the sum of all anti-clockwise oriented tunneling paths defines an MPO

$$\hat{O}_+^{(6)} = \frac{63}{8E_C^5} \text{Tr} \left(\hat{B}^1 \hat{B}^2 \hat{B}^3 \right), \quad (46)$$

with MPO matrix elements

$$\begin{aligned} \hat{B}_{00}^i &= -\alpha_i(a_i \hat{x} \otimes \hat{x} + b_i \hat{y} \otimes \hat{y}), \\ \hat{B}_{01}^i &= \beta_i(a_i \hat{x} \otimes \hat{y} - b_i \hat{y} \otimes \hat{x}), \\ \hat{B}_{10}^i &= \alpha_i(a_i \hat{y} \otimes \hat{x} - b_i \hat{x} \otimes \hat{y}), \\ \hat{B}_{11}^i &= -\beta_i(a_i \hat{y} \otimes \hat{y} + b_i \hat{x} \otimes \hat{x}), \end{aligned} \quad (47)$$

acting on the repetition qubits. Using the above restrictions $a_i = -b_i$, $\alpha_i = \pm i\beta_i$,

$$\begin{aligned} \hat{B}_{11}^i &= \pm iB_{00}^i = c_i(\hat{x} \otimes \hat{x} - \hat{y} \otimes \hat{y}), \\ \hat{B}_{01}^i &= \mp iB_{10}^i = c_i(\hat{x} \otimes \hat{y} + \hat{y} \otimes \hat{x}), \end{aligned} \quad (48)$$

with the so far freely adjustable coefficient $c_i := \beta_i a_i$. We finally need to choose these parameters such that the sum of the oriented path and its Hermitian conjugate (the reversed path) reproduces the action of $-\hat{X}$ in (44). A straightforward calculation shows that this is the case for e.g. $c_i = i$ and $\alpha_i = i\beta_i$. With this choice, the relatively simply MCB network defines an effective tunneling Hamiltonian, \hat{H}_v which encodes the essential structure of the double semion vertex.

Bell pair bridges and double semion network — In a final step, we couple individual vertex structures via Bell bridges as in Fig. 10. These couplings shown in Fig. 17 are to generate a locking of the virtual states of neighboring vertices to a Bell state according to the geometry of the tensor network in Fig. 14. The coupling effectively assigns a Bell pair Hamiltonian, \hat{H}_{Bell} [Eq. (29)], to all (doubled) edges of the underlying honeycomb lattices connecting two vertices [72].

Note that \hat{H}_{Bell} is generated by length-2 loops while the tunneling loops within each triangle — driving the system to the code space — are of length six and thus *a priori* weaker. To ensure that the Bell pair Hamiltonians can nonetheless be treated as a perturbation, the respective tunneling strengths λ_{Bell} should be sufficiently small ensuring that $\varepsilon := \lambda_{\text{Bell}}^2/E_C$ is small. The effective Hamiltonian of the whole MCB network is given by

$$\hat{H}_{\text{eff}} = \sum_v \hat{H}_v + \varepsilon \sum_e \hat{H}_{\text{Bell}} + \mathcal{O}(\varepsilon \lambda^2/E_C^2), \quad (49)$$

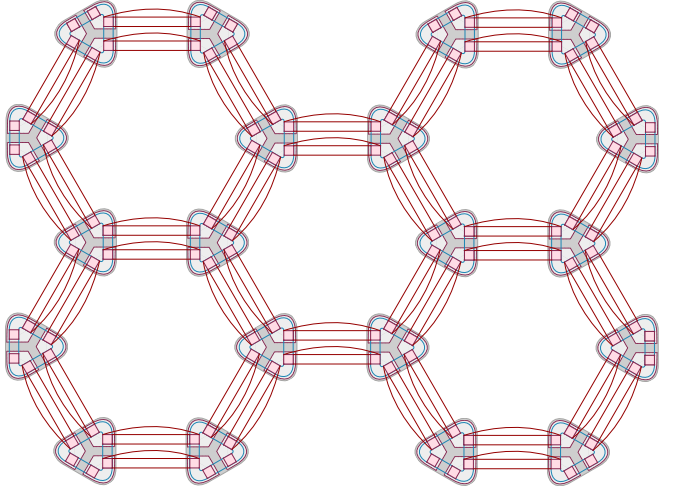


FIG. 17. Double semion MCB network: Triangular 6-tetron vertices (grey triangles), see Fig. 16, are connected via Bell pair tunneling bridges (red). Note that vertices are arranged in two different sub-lattices. For a magnified view of the coupling between vertices, see Fig. 18 below.

where λ is the absolute value of the tunneling amplitudes a_i, b_i and the leading corrections represent inter-vertex loops of length four, which are parametrically weaker than the leading contributions. In addition they can be controlled to such an extent that they do not influence the result of the perturbative analysis [73] of the Hamiltonian in Eq. (38). As a conclusion the above effective Hamiltonian has the same ground state space as the perturbative PEPS parent in Eq. (38). Details of the perturbation series analysis are provided in the Appendix.

Practical implementation — Fig. 17 shows a schematic of the actual hardware layout implementing the construction. The discussion above reflects the importance of an initial calibration procedure which in turn necessitates the presence of local gates near each tunneling link. Specifically, starting from a configuration in which the (b_i, β_i) are turned off, interferometric measurements [30, 31] between all possible Majorana pair combinations around the outer loop defined by the (a_i, α_i) links, followed by subsequent gate voltage tuning, will be applied to fix a possible choice of relative coupling amplitudes $a_i = -\alpha_i = \lambda$ with λ real. In the next step, interferometric measurements and gate voltage readjustments are carried out for each length-2 loop defined by (a_i, b_i) and (α_i, β_i) until one has achieved the values of $b_i = -a_i$ and $\beta_i = ia_i$, such that we obtain $c_i = i\lambda^2$ and λ^2 is an inconsequential proportionality factor to the value specified above. In view of the presumed robustness of the topological phases, we do not expect that excessive precision need be applied in these calibration steps. At any rate, they would be performed in an automated manner.

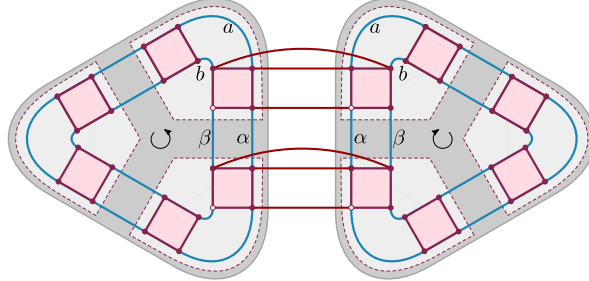


FIG. 18. Bell pair tunnel bridges connecting neighboring vertices in the double semion MCB network of Fig. 17.

V. CONCLUSIONS AND OUTLOOK

In this work, tensor network approaches have been introduced for quantum simulations of complex phases of matter in networks of Majorana Cooper boxes. Such networks may be experimentally realizable in the near future. We have formulated several design principles generating desired many-qubit interactions, and suppressing unwanted lower-order interactions via mechanisms of symmetry or engineered destructive interference. Specifically, we have studied how tensor networks may serve to simulate topological Levin-Wen string-net models [2, 7] beyond Kitaev's toric code, a class of systems so far elusive. As a concrete example, we have detailed how to simulate the ground state of the double semion model [7], the simplest string-net beyond the toric code. While the quantum simulation of an exactly solvable model in its pristine form may provide only limited insights, our constructions allow to perturb around the solvable limit in controlled ways and probe the stability of the phase. Similarly, the realization of the net will be a first and necessary step to the creation of excitations and the study of their dynamics.

The present work illustrates the potential of the linkage condensed-matter/tensor network/device implementation, and may actually define an entire research program. Concrete directions of research within the general framework include the realization of a large class of many-qubit interactions from correlated Majorana Cooper box networks, or novel quantum simulation schemes [9, 10] with read-out possibilities [30, 31] unavailable in other architectures. It should be clear that the local multi-qubit interactions generated by networks of Majorana Cooper boxes as such already hold the promise of establishing new quantum simulation schemes, regardless of notions of topological order.

In this work, we have gone further to show how to engineer a restricted class of matrix product operators with bond dimension $D = 2$, where network structures emerge by building on Hamiltonian gadget techniques. However, one may go beyond the level of tetrions to design hexon or polygon networks of advanced flexibility and versatility. At any rate, it will be important to extend the scope and to understand in generality which types of matrix product operators can be designed in such architectures. The flexibility of the Majorana platform may in fact allow for large classes of matrix product operators while avoiding undesired few-qubit interactions.

However, further research is required to substantiate this expectation.

Turning to applications, it will be exciting to explore other phases of matter that can be simulated within the present framework. For example, the Majorana dimer models [74, 75] are a class of systems which appear to be within direct reach. From the perspective of quantum information, realizing Fibonacci anyon models [7] and exploring implications for topological quantum computing is an obvious stepping stone. Given the huge overhead in surface code based topological quantum computing using Clifford operators and magic state distillation [4], a comprehensive analysis of such alternative approaches seems highly desirable. We are confident that our work will also stimulate research along this direction.

ACKNOWLEDGMENTS

We warmly thank A. Bauer for various helpful discussions and acknowledge funding by the DFG (CRC TR 183 within project C4 and EI 519/7-1), the Studienstiftung des Deutschen Volkes, and the ERC (TAQ).

Note added: During the writing of this manuscript, we became aware of two interesting preprints [76, 77] suggesting the application of MCB networks to the quantum simulation of spin liquid phases. These works, too, exploit the freedom of engineered interactions in Majorana networks. However, the focus is more on generating tailored spin correlations, and the design principles of tensor networks or string-net phases are not considered.

Appendix: Perturbation analysis

We consider the MCB network in Fig. 17 with the Hamiltonian in Eq. (49), where we assume that the energy scale λ^6/E_C^5 characterizing the vertex part, \hat{H}_v , is much larger than the scale $\varepsilon = \lambda_{\text{Bell}}^2/E_C$ corresponding to Bell pair tunneling links between neighboring vertices. Under this assumption, the analysis of Ref. [59] applies where one treats the Bell pair Hamiltonians \hat{H}_{Bell} as perturbation to $\sum_v \hat{H}_v$. In addition, in our case, terms of order $\mathcal{O}(\varepsilon \lambda^2/E_C^2)$ arise due to loops of length 4 (and beyond) which involve MCBs on different vertices. Such contributions need to be included in a perturbative analysis aimed at checking that the low-energy Hamiltonian of the perturbative PEPS parent theory is indeed the parent Hamiltonian of the encoded PEPS, Eq. (37). While the full analysis combining global and local Schrieffer-Wolff transformations [57] is cumbersome, a simplified calculation [73] for the double semion model considers a self-energy expansion series order by order and establishes the physical meaning of each term. As in our perturbative expansion for the low-energy physics of MCB networks in Sec. II, only operators acting within the ground state space of the dominant Hamiltonian term, here the code space, are considered.

The first order gives no contribution since $\hat{P}\hat{H}_{\text{Bell}}\hat{P} = 0$, where \hat{P} is the projector to the ground state of $\sum_v \hat{H}_v$. In fact, all odd orders do not contribute apart from trivial energy

shifts. At second order, the simultaneous action of Bell pair operators on two neighboring vertices yields a contribution favoring even parity states for the corresponding four qubits. This term has a clear physical meaning. Indeed, mapping the encoded state back to the physical state by applying the PEPS map A , one finds that the physical state (which used to live on the edge of the honeycomb lattice) is overdetermined. Thanks to the even parity constraint for the four qubits, this over-determination is resolved and one recovers a consistent mapping from code space to physical space. At fourth order, products of second-order terms but no qualitatively new contributions emerge. Such contributions arise, however, in sixth order from six Bell pairs Hamiltonians acting on 12 qubits around one plaquette. These terms correspond to encoded versions of the string-net plaquette operator and are essential to drive the system into a topological phase. Note that up to the fifth order, the effective Hamiltonian only contains (encoded versions of) vertex projections and terms ensuring consistency of different local decodings, where one does not expect a topologically ordered ground state. It is thus crucial that the effect of the plaquette operator is relevant for the system. In particular, if we repeat the perturbative analysis for the MCB network Hamiltonian, taking into account perturbations due to loops of length 4 and beyond, we have to check that no terms overwhelming the plaquette operator are present which can potentially destroy the topological order of the ground state.

The design of the MCB network in Sec. IV C overcomes this obstacle in a natural way by making use of destructive interference mechanisms. Consider a junction of two vertices connected by two Bell pair bridges in Fig. 18. There are 36 different length-4 loops that emerge from tunneling from one MCB at one vertex to the neighboring MCB on the same vertex (via α or β) then to the other vertex via one of the three Bell bridges, then (again via α or β) to the neighboring MCB and finally back to the starting point via one of the three Bell bridges. It is useful to partition these 36 loops into four different groups labeled by the loop phase $\phi_{\alpha/\beta} - \phi_{\alpha/\beta}$. Let us analyse the different $\phi_\alpha - \phi_\beta$ loops. There is one loop that

is threatening the emergence of topological order. It corresponds to the $\hat{z}\hat{z}$ interactions on neighboring qubits, interactions that we needed to suppress already in the design of the vertex Hamiltonian. Because the parity of two different corner qubits determines the physical state uniquely, a system that favors a specific parity of those two qubits corresponds to a trivial product state. Since this state is part of the code space there is no chance to argue that it will not survive the code space projection P . This is why we have chosen the tunneling links on different sublattices according to Fig. 18. The loop phase $\phi_\alpha - \phi_\beta = \pi/2$ and likewise $\phi_\beta - \phi_\alpha$ leads to a complete cancellation of all those loops (note that the Bell pair wires don't add phase shifts) including the one that would otherwise lead to the adverse $\hat{z}\hat{z}$ interaction. The other half of the length-4 loops does not vanish but also poses no threat to the formation of topological order. They are of the form $\hat{O}^{(4)} \propto \hat{p}\hat{p} \otimes \hat{q}\hat{q}$ where the tensor product indicates the separation into two Bell pairs and \hat{p}, \hat{q} denote different Pauli operators. Contributions of this form also arise in second order perturbation theory in ε from the Bell pair Hamiltonian and therefore do not yield qualitatively new contributions. In addition they are completely outside the code space and do not contribute at all when treated as a first order correction to $\sum_v H_v$. Similar arguments apply to higher order loop terms. Prominently among them are detour-loops that wind once around a vertex ring but with a detour via two qubits of a neighboring vertex. Those detour terms either leave the code space or yield terms that correspond to a product of $O^{(6)}$ and $\hat{z}\hat{z} \otimes \hat{z}\hat{z}$. These terms cause a splitting of the ground state space degeneracy that is in agreement with the aforementioned consistency of physical qubit states and do not cause a phase transition. Detour terms involving more than one detour can be treated similarly.

To conclude, we have verified that the analysis of Ref. [73], and therefore our encoded PEPS approach to the ground state of the double semion model, also applies in the presence of higher-order terms of $\mathcal{O}(\varepsilon\lambda^2/E_C^2)$ in Eq. (49).

-
- [1] C. Nayak, S. H. Simon, A. Stern, M. Freedman, and S. Das Sarma, *Rev. Mod. Phys.* **80**, 1083 (2008).
 - [2] X. G. Wen, *Rev. Mod. Phys.* **89**, 041004 (2017).
 - [3] E. Dennis, A. Kitaev, A. Landahl, and J. Preskill, *J. Math. Phys.* **43**, 4452 (2002).
 - [4] S. Bravyi and A. Kitaev, *Phys. Rev. A* **71**, 022316 (2005).
 - [5] A. Y. Kitaev, *Ann. Phys.* **303**, 2 (2003).
 - [6] B. M. Terhal, *Rev. Mod. Phys.* **87**, 307 (2015).
 - [7] M. Levin and X. G. Wen, *Phys. Rev. B* **71**, 045110 (2005).
 - [8] M. Levin and X.-G. Wen, *Phys. Rev. Lett.* **96**, 110405 (2006).
 - [9] J. I. Cirac and P. Zoller, *Nature Phys.* **8**, 264 (2012).
 - [10] A. Acin, I. Bloch, H. Buhrman, T. Calarco, C. Eichler, J. Eisert, D. Esteve, N. Gisin, S. J. Glaser, F. Jelezko, S. Kuhr, M. Lewenstein, M. F. Riedel, P. O. Schmidt, R. Thew, A. Wallraff, I. Walmsley, and F. K. Wilhelm, (2017), arXiv:1712.03773.
 - [11] R. Orús, *Ann. Phys.* **349**, 117 (2014).
 - [12] J. Eisert, M. Cramer, and M. B. Plenio, *Rev. Mod. Phys.* **82**, 277 (2010).
 - [13] F. Verstraete, J. I. Cirac, and V. Murg, *Adv. Phys.* **57**, 143 (2008).
 - [14] N. Schuch, Lecture notes for the 44th IFF Spring School “Quantum Information Processing” in Juelich (2013).
 - [15] J. Alicea, *Rep. Prog. Phys.* **75**, 076501 (2012).
 - [16] M. Leijnse and K. Flensberg, *Semicond. Sci. Technol.* **27**, 124003 (2012).
 - [17] C. W. J. Beenakker, *Annu. Rev. Con. Mat. Phys.* **4**, 113 (2013).
 - [18] S. D. Sarma, M. Freedman, and C. Nayak, *njp Quant. Inf.* **1**, 15001 (2015).
 - [19] R. Aguado, *Rivista del Nuovo Cimento* **40**, 523 (2017).
 - [20] R. M. Lutchyn, E. P. A. M. Bakkers, L. P. Kouwenhoven, P. Krogstrup, C. M. Marcus, and Y. Oreg, *Nat. Rev. Mat.* **3**, 52 (2017).
 - [21] V. Mourik, K. Zuo, S. M. Frolov, S. R. Plissard, E. P. A. M. Bakkers, and L. P. Kouwenhoven, *Science* **336**, 1003 (2012).
 - [22] S. M. Albrecht, A. P. Higginbotham, M. Madsen, F. Kuemmeth, T. S. Jespersen, J. Nygård, P. Krogstrup, and C. M. Marcus,

- Nature* **531**, 206 (2016).
- [23] M. T. Deng, S. Vaitiekėnas, E. B. Hansen, J. Danon, M. Leijnse, K. Flensberg, J. Nygård, P. Krogstrup, and C. M. Marcus, *Science* **354**, 1557 (2016).
- [24] F. Nichele, A. C. C. Drachmann, A. M. Whiticar, E. C. T. O’Farrell, H. J. Suominen, A. Fornieri, T. Wang, G. C. Gardner, C. Thomas, A. T. Hatke, P. Krogstrup, M. J. Manfra, K. Flensberg, and C. M. Marcus, *Phys. Rev. Lett.* **119**, 136803 (2017).
- [25] S. Gazibegovich, D. Car, H. Zhang, S. C. Balk, J. A. Logan, M. W. A. de Moor, M. C. Cassidy, R. Schmits, D. Xu, G. Wang, P. Krogstrup, R. L. M. Op het Veld, J. Shen, D. Bouman, B. Shojaei, D. Pennachio, J. S. Lee, P. J. van Veldhoven, S. Koelling, M. A. Verheijen, L. P. Kouwenhoven, C. J. Palmstrøm, and E. P. A. M. Bakkers, *Nature* **548**, 434 (2017).
- [26] H. Zhang, C. X. Liu, S. Gazibegovich, D. Xu, J. Logan, G. Wang, N. van Loo, J. D. S. Bommer, M. W. A. de Moor, D. Car, R. L. M. Op het Veld, P. J. Veldhoven, S. Koelling, M. A. Verheijen, C. J. Palmstrøm, M. Pendharkar, D. J. Pennachio, B. Shojaei, J. S. Lee, E. P. A. M. Bakkers, and L. P. Kouwenhoven, *Nature* **556**, 74 (2018).
- [27] B. Béri and N. R. Cooper, *Phys. Rev. Lett.* **109**, 156803 (2012).
- [28] B. Béri, *Phys. Rev. Lett.* **110**, 216803 (2013).
- [29] A. Altland and R. Egger, *Phys. Rev. Lett.* **110**, 196401 (2013).
- [30] S. Plugge, A. Rasmussen, R. Egger, and K. Flensberg, *New J. Phys.* **19**, 012001 (2017).
- [31] T. Karzig, C. Knapp, R. M. Lutchyn, P. Bonderson, M. B. Hastings, C. Nayak, J. Alicea, K. Flensberg, S. Plugge, Y. Oreg, C. M. Marcus, and M. H. Freedman, *Phys. Rev. B* **95**, 235305 (2017).
- [32] Z.-C. Gu, M. Levin, B. Swingle, and X.-G. Wen, *Phys. Rev. B* **79**, 085118 (2009).
- [33] O. Buerschaper, M. Aguado, and G. Vidal, *Phys. Rev. B* **79**, 085119 (2009).
- [34] N. Schuch, M. M. Wolf, F. Verstraete, and J. I. Cirac, *Phys. Rev. Lett.* **100**, 030504 (2008).
- [35] M. B. Sahinoglu, D. Williamson, N. Bultinck, M. Marien, J. Haegeman, N. Schuch, and F. Verstraete, [arxiv:1409.2150](https://arxiv.org/abs/1409.2150).
- [36] D. J. Williamson, N. Bultinck, J. Haegeman, and F. Verstraete, [arXiv:1609.02897](https://arxiv.org/abs/1609.02897).
- [37] C. Wille, O. Buerschaper, and J. Eisert, *Phys. Rev. B* **95**, 245127 (2017).
- [38] S. Vijay, T. H. Hsieh, and L. Fu, *Phys. Rev. X* **5**, 041038 (2015).
- [39] L. A. Landau, S. Plugge, E. Sela, A. Altland, S. M. Albrecht, and R. Egger, *Phys. Rev. Lett.* **116**, 050501 (2016).
- [40] S. Plugge, L. A. Landau, E. Sela, A. Altland, K. Flensberg, and R. Egger, *Phys. Rev. B* **94**, 174514 (2016).
- [41] B. M. Terhal, F. Hassler, and D. P. DiVincenzo, *Phys. Rev. Lett.* **108**, 260504 (2012).
- [42] D. Aasen, M. Hell, R. V. Mishmash, A. Higginbotham, J. Danon, M. Leijnse, T. S. Jespersen, J. A. Folk, C. M. Marcus, K. Flensberg, and J. Alicea, *Phys. Rev. X* **6**, 031016 (2016).
- [43] F. Verstraete and J. I. Cirac, [cond-mat:0407066](https://arxiv.org/abs/0407066).
- [44] H. N. Phien, J. A. Bengua, H. D. Tuan, P. Corboz, and R. Orus, *Phys. Rev. B* **92**, 035142 (2015).
- [45] S. R. White, *Phys. Rev. Lett.* **69**, 2863 (1992).
- [46] N. Schuch, D. Poilblanc, J. I. Cirac, and D. Perez-Garcia, *Phys. Rev. Lett.* **111**, 090501 (2013).
- [47] N. Schuch, J. I. Cirac, and D. Perez-Garcia, *Ann. Phys.* **325**, 2153 (2010).
- [48] N. Schuch, D. Perez-Garcia, and I. Cirac, *Phys. Rev. B* **84**, 165139 (2011).
- [49] F. Pollmann, A. M. Turner, E. Berg, and M. Oshikawa, *Phys. Rev. B* **81**, 064439 (2010).
- [50] C. Xu and L. Fu, *Phys. Rev. B* **81**, 134435 (2010).
- [51] A. Roy, B. M. Terhal, and F. Hassler, *Phys. Rev. Lett.* **119**, 180508 (2017).
- [52] Z. Nussinov, G. Ortiz, and E. Cobanera, *Phys. Rev. B* **86**, 085415 (2012).
- [53] S. Vijay and L. Fu, *Phys. Rev. B* **94**, 235446 (2016).
- [54] D. Litinski, M. S. Kesselring, J. Eisert, and F. v. Oppen, *Phys. Rev. X* **7**, 031048 (2017).
- [55] L. Fu, *Phys. Rev. Lett.* **104**, 056402 (2010).
- [56] T. Hyart, B. van Heck, I. C. Fulga, M. Burrello, A. R. Akhmerov, and C. W. J. Beenakker, *Phys. Rev. B* **88**, 035121 (2013).
- [57] S. Bravyi, D. P. DiVincenzo, and D. Loss, *Ann. Phys.* **326**, 2793 (2011).
- [58] L. Fidkowski, M. Freedman, C. Nayak, K. Walker, and Z. Wang, *Comm. Math. Phys.* **287**, 805 (2009).
- [59] C. G. Brell, S. D. Bartlett, and A. C. Doherty, *New J. Phys.* **16**, 123056 (2014).
- [60] F. Verstraete, J. J. Garcia-Ripoll, and J. I. Cirac, *Phys. Rev. Lett.* **93**, 207204 (2004).
- [61] B. Pirvu, V. Murg, J. I. Cirac, and F. Verstraete, *New J. Phys.* **12**, 025012 (2010).
- [62] M. Fannes, B. Nachtergaele, and R. Werner, *Commun. Math. Phys.* **144**, 443 (1992).
- [63] B. Pirvu, V. Murg, J. I. Cirac, and F. Verstraete, *New J. Phys.* **12**, 025012 (2010).
- [64] M. Kliesch, D. Gross, and J. Eisert, *Phys. Rev. Lett.* **113**, 160503 (2014).
- [65] N. Bultinck, M. Marien, D. Williamson, M. B. Sahinoglu, J. Haegeman, and F. Verstraete, *Ann. Phys.* **378**, 183 (2017).
- [66] O. Buerschaper, S. C. Morampudi, and F. Pollmann, *Phys. Rev. B* **90**, 195148 (2014).
- [67] A. Y. Kitaev, *Ann. Phys. (N.Y.)* **303**, 2 (2003).
- [68] N. E. Bonesteel and D. P. DiVincenzo, *Phys. Rev. B* **86**, 165113 (2012).
- [69] P. Fendley, S. V. Isakov, and M. Troyer, *Phys. Rev. Lett.* **110**, 260408 (2013).
- [70] N. Schuch, I. Cirac, and D. Perez-Garcia, *Ann. Phys.* **325**, 2153 (2010).
- [71] O. Buerschaper, *Ann. Phys.* **351**, 447 (2014).
- [72] For completeness, we mention that the coupling always connects vertices of different sublattices. For a connection as indicated in the Fig. 18, the right triangle is identical to the one above. A closer inspection shows that the difference between the operator representing the left triangle differs from the one on the right by interchanging a vs b and α vs β which yields a replacement $\hat{B}_{00} \mapsto \hat{B}_{11}$, $\hat{B}_{11} \mapsto \hat{B}_{00}$, $\hat{B}_{01} \mapsto -\hat{B}_{10}$, $\hat{B}_{10} \mapsto -\hat{B}_{01}$ in Eq. (48). However, since the B_{01} , B_{10} always appear in pairs, the MPO O_6 is the same.
- [73] C. G. Brell, S. Burton, G. Dauphinais, S. T. Flammia, and D. Poulin, *Phys. Rev. X* **4**, 031058 (2014).
- [74] N. Tarantino and L. Fidkowski, *Phys. Rev. B* **94**, 115115 (2016).
- [75] B. Ware, J. H. Son, M. Cheng, R. V. Mishmash, J. Alicea, and B. Bauer, *Phys. Rev. B* **94**, 115127 (2016).
- [76] E. Sagi, H. Ebisu, Y. Tanaka, A. Stern, and Y. Oreg, preprint (2018), [arXiv:1806.03304](https://arxiv.org/abs/1806.03304).
- [77] A. Thomson and F. Pientka, (2018), [arXiv:1807.09291v1](https://arxiv.org/abs/1807.09291v1).